

DELFT UNIVERSITY OF TECHNOLOGY

BACHELOR THESIS

AESB 3400

**Quantified Characterization of Discrete Fractures
through Surface Roughness, Surface Area, and
Hydraulic Conductivity**

Author: Cornelis Reijm
(4647513)

July 5, 2021



Preface

My sincerest thanks to my supervisors Dr. Anne-Catherine Dieudeonne and Dr. Auke Barnhoorn and B. Malagar for their giving their advice and feedback when I asked and needed it. It is thanks to you that I have been thoroughly introduced into such a wonderful multi-faceted topic. I would also like to thank my family for their constant support throughout these last three years that has sustained me and maintained a general peace of mind.

Student number: 4647513
Project duration: March 1, 2012 – January 1, 2013
Thesis committee: Dr. ir. A.A.M. (Anne-Catherine) Dieudonne, TU Delft, supervisor
Dr. A. (Auke) Barnhoorn, TU Delft, supervisor
B. (Bhini) Malagar (MSc)
Institution: Delft University of Technology
Faculty: Civil Engineering and Geosciences
Section: Geo-engineering

Contents

- 1 Introduction** **1**
- 1.1 Purpose and Scope 1
- 1.2 Opalinus Clay 2
- 1.3 Self-sealing Mechanisms 3
- 1.4 Terminology and Morphological Descriptors 4

- 2 Methodology** **6**
- 2.1 2D Descriptor Analysis 6
 - 2.1.1 Amplitude 6
 - 2.1.2 Amplitude Density 7
 - 2.1.3 Bearing Area Curve 8
- 2.2 3D Descriptor Analysis 9
- 2.3 Surface Area 9
- 2.4 Hydraulic Conductivity 11

- 3 Results** **13**
- 3.1 Interpretation 13
 - 3.1.1 Opalinus Clay Sample 1 13
 - 3.1.2 Opalinus Clay Sample 2 18
- 3.2 Surface Area 24
- 3.3 Hydraulic Conductivity 26

- 4 Discussion** **27**
- 4.1 Uncertainties in hydraulic conductivity 27
- 4.2 Uncertainties in Quantifying Surface Area 29
- 4.3 2D and 3D Descriptor Analysis 29
- 4.4 Future Development 30

- 5 Conclusion** **32**

- A Opalinus Claystone Samples** **33**

- B Graphical Relationships** **35**

Abstract

Argillaceous (clay-rich) host formations for radioactive waste geological repositories are extensively researched for their capability to decrease the hydraulic conductivity of fractures over time (i.e. self-sealing). This self-sealing behavior is beneficial in the context of radioactive repositories as the excavation of these spaces unavoidably induce fractures in a region called the excavation damaged zone (EDZ), allowing for radioactive particles to leak into the surrounding environment and groundwater. Despite knowing the mechanisms for self-sealing (e.g. swelling of clay minerals), more research is needed into the complexities of self-sealing to fully understand and effectively utilize it widely. To facilitate research of swelling in induced fractures, a quantified method of fracture characterization using morphological descriptors is developed to provide insight into the morphological state of the fracture surface and its influence on the self-sealing capacities of argillaceous rocks. This was carried out by identifying morphological descriptors of a rough surface and their relation to roughness, as it pertains to macroscopic and microscopic roughness. A dynamic script was developed capable of: analyzing and quantifying morphological descriptors of roughness in 2 and 3-dimensions, calculating the surface area of a rough surface, and calculating hydraulic conductivities (k_x and k_y) of a discrete fracture. This method was tested using two samples of Opalinus Clay (OPA) from the Mont Terri underground research laboratory (URL) in Switzerland. Furthermore, derived data of heterogeneous morphology, along with surface area and hydraulic conductivity, is used to discuss the limitations and constraints of the developed method and compare 2-dimensional versus 3-dimensional morphological analysis to determine what combination of analysis fully captures the breadth of morphological information. It was determined that the morphological descriptors of amplitude, amplitude density, and the bearing area curve (BAC) are suitable descriptors to define the microscopic and macroscopic roughness of a rough surface, where both forms of roughness are defined in the context of influence from local maximums (asperities) and local minimums (valleys) of the surface. Comparison of the 2 and 3-dimensional analyses of these morphological descriptors shows that a combination of the 2D BAC, 3D amplitude, and 2D amplitude densities both fully capture the breadth of morphological information and provide an easier means of interpretation. Using Delaunay triangulation on the surfaces of both OPA samples, the calculated upper and lower bounds of surface area for sample 1 is: 2267.37mm² and 942.09mm² and is: 2377.64mm² and 959.73mm² for sample 2. Compared to the planar surface area of each OPA sample analyzed, this corresponds to an 847 - 2039% increase for OPA sample 1 and a 998 - 2399% increase in surface area for OPA sample 2. The calculated hydraulic conductivities k_x and k_y for sample 1 is: 1.78×10^{-7} m/s and 7.75×10^{-7} m/s and is: 8.01×10^{-9} m/s and 2.1×10^{-7} m/s for sample 2. This is compared to the hydraulic conductivity of the Opalinus clay material, which is 2×10^{-13} m/s. Future research into discrete fracture characterization using morphological descriptors should focus on increasing the computational efficiency of the existing code, improving the surface area calculations, and transforming the matrices of data into one points of data for easier comparison of discrete fractures across multiple samples. In doing so, it is hoped that this small contribution will aid in understanding morphology influence on swelling development in induced fractures in argillaceous geomaterial.

1 Introduction

1.1 Purpose and Scope

The waste management of radioactive material is a serious issue in which many considerations are made. Radioactive waste material must be stored within safe repositories where the radioactive material can decay over time. As such, repositories made for radioactive waste must be isolated and have very low permeabilities (Levasseur et al., 2020; Bock et al., 2010; Pluymakers et al., 2017; Akono and Kabir, 2016). Within the past five decades, argillaceous geomaterials, namely claystones, have been investigated as potential host formations for the siting of deep subsurface radioactive waste repositories. There does however exist an inherent problem in excavating a subsurface geological repository, namely that the excavation process itself results in fracturing of the surrounding rocks in a region called the excavation damaged zone (EDZ). The removal of rock from the whole rock mass unit causes a variable change in stress that, when redistributed, results in effective normal stresses perpendicular to the free surface of the excavated zone and strain within the rock mass. Fractures develop to accommodate for the strain, whose mode and orientation are dependent upon the initial and local stress field that results after redistribution. The three modes of fracture development are tensile opening (mode I), in-plane shearing (mode II), and out-of-plane shearing (mode III). All three modes are modelled as a discrete fracture that comprises a larger network of discrete fractures called the discrete fracture network (DFN) (Bock et al., 2010; Levasseur et al., 2020). Fractures in the EDZ essentially negate the quasi-impermeable nature of clay-rich rocks, and it begs the question as to why argillaceous rocks are considered a viable candidate for a repository material. Argillaceous geomaterials display a unique phenomenon to close discontinuities with the passage of time, and thereby reducing the transmissivity of the material back toward its original in-situ condition (i.e. self-sealing) (Bock et al., 2010; Levasseur et al., 2020; Pluymakers et al., 2017).

To further understand and utilize argillaceous self-sealing within geotechnical engineering applications, further research is required into the finer complexities of self-sealing as it should be fully understood before using it for large scale radioactive waste disposal. Ignoring or under-utilizing self-sealing, within the context of radioactive waste repositories, could potentially lead to leakage of radionuclides and lead to catastrophic consequences. To contribute toward the further understanding of argillaceous geomaterials and their self-sealing behavior, a quantitative fracture characterization method is made to facilitate the future research of self-sealing within Opalinus clay via swelling, which will be conducted by Dr.ir. (Anne-Catherine) A.A.M. Dieudonne. This fracture characterization method analyzes descriptors of the fracture surface in 2 and 3 dimensions to determine morphology and hydraulic permeability of a discrete fracture. The hydraulic permeability quantification method is best modeled by a DFN, whose geometric properties influence the transmissivity through an individual fracture (Zou, 2020; Zambrano et al., 2019; Tatone and Grasselli, 2015). These geometric properties are the aperture and roughness of a given discontinuity, with roughness being described by morphological descriptors. It is important to note that this characterization is performed on millimeter scale samples of Opalinus Clay (OPA), whose face was part of a discontinuity within a larger rock mass. Despite the discontinuity samples not originating from a fracture, its similarity in descriptors to that of a fracture surface makes it a suitable surrogate for fracture characterization.

It is the aim and intent of this this research to develop a method of quantifying roughness, surface area and hydraulic conductivity, thereby characterizing a discrete fracture with morphological descriptors. As such, this thesis will identify morphological descriptors and explain their relevance in the context of fracture roughness and determine which dimension of analysis is best for each descriptor. In doing so, the level and type of information needed to sufficiently characterize the morphology of a rough surface is identified, which, in tandem with surface area and hydraulic permeability, leads to a more efficient characterization method. To achieve the aims and goals of this thesis, literature pertaining to fracture characterization, surface roughness, and fracture transmissivity were analyzed. From this analysis, methods to quantify and characterize the discrete fracture through morphological descriptors were implemented into a working script via *Python*. The remainder of this thesis details the specific methodology, results and derivations, and is as follows. Section 2 details the methods of analysis for each descriptor (in 2 and 3-dimensions), the surface area and hydraulic permeability, briefly mentioning limitations and constraints to each analysis. Section 3 presents the results for each analysis and uses observations from these results to make an interpretation of each OPA sample as it pertains to roughness. Both the results and the interpretations act as a proof of concept for the developed method of fracture characterization based on morphological

descriptors. Section 4 discusses 2 and 3-dimensional descriptor analysis and the limitations and uncertainties for surface area and hydraulic permeability quantification, as well as future contributions that can be made to improve the applicability and potency of the developed method. Section 5 restates the aims and goals of this thesis, stating its significance and briefly summarizing conclusions made.

1.2 Opalinus Clay

The samples used within this thesis are made from Opalinus Clay and were obtained from the Mont Terri underground research laboratory (URL) in Switzerland where extensive research is conducted into the self-sealing and mechanical properties of this geomaterial. The samples are shown in Figure 1 with a 1 Euro coin for scale. OPA formed approximately 175 million years ago in the Jurassic Period and resulted from sedimentation of marine clay into a shallow-marine epicontinental sea in central Europe over the course of 400,000 years (Kneuker and Furche, 2021; Lauper et al., 2021). The OPA vary in mineralogical and organic content depending on the facies (e.g., carbonate-rich sandy facies) (Kneuker and Furche, 2021; Lauper et al., 2021), but the composition of the samples used are known. 55% by weight of the OPA from Mont Terri is non-swelling minerals, namely kaolinite and chlorite, while 10% by weight is composed illite and smectite. Illite and smectite are swelling minerals, which are main contributors to self-sealing in argillaceous geomaterial and is discussed further in Section 1.3. The swelling capacity of this material is 7-9%, but the material will disintegrate and turn into a paste if cyclically wetted and dried multiple times. It is also important to note the hydraulic conductivity of the non-fractured material, which is 2×10^{-13} m/s.



(a) Sample 1

(b) Sample 2

Figure 1: *Opalinus clay samples used within the thesis to test the developed method of characterization. The samples are shown next to 1 euro coin for scale.*

1.3 Self-sealing Mechanisms

Self-sealing is investigated in underground research laboratories, most notably in the Mont Terri, Meuse/Haute-Marne and HADES URLs that are in Switzerland, France and Belgium, respectively (Bock et al., 2010; Levasseur et al., 2020; Corkum and Martin, 2007). In conducting self-sealing research, the mechanisms for self-sealing capability are investigated and documented. From extensive documentation, it is well established that the causes for self-sealing within argillaceous media are: mechanical closure, swelling, uniform compaction, clogging by comminution, and mineral precipitation (Bock et al., 2010; Levasseur et al., 2020; Pluymakers et al., 2017). As fracture characterization, and by extension self-sealing, is discussed and considered within the context of a subsurface repository, mineral precipitation is not further discussed as repository sites are generally hydro-thermally and tectonically quiet (Bock et al., 2010). Furthermore uniform compression will not be discussed nor considered as this mode of self-sealing is of least importance (Bock et al., 2010; Levasseur et al., 2020). As such, only mechanical closure, swelling, and fracture clogging are relevant within the predefined context. It is important to note that the self-sealing only refers to recovery of the hydraulic properties of the Opalinus clay (OPA) and not the mechanical properties of the OPA. Any argillaceous rock within the EDZ that is self-sealed does not forget the stress history and still maintains a state of mechanical failure. The phenomenon of discontinuity closure and regaining the natural undisturbed material properties and strength is referred to as self-healing, which is not discussed within this thesis.

Mechanical closure is the induced closure of cracks and fractures due to effective stresses acting on the fracture and is achieved by either normal stress, shear stress, or creep (Bock et al., 2010; Levasseur et al., 2020). These induced loads on the fracture, either induced or naturally over time (in the case of creeping), alter the existing stress field to forcibly close the fracture, thereby decreasing the transmissivity of the fracture. In the case of shear stresses, it may also result that increased stress on the fracture causes a dilation of the fracture as asperities (i.e. surface bumps) sit on top of each other, rather than interlocking with each other. Though, this dilating behavior is dependent upon the shear strength and geometry of the asperities for both surfaces (Bock et al., 2010; Levasseur et al., 2020). If the shear stress on the fracture overcomes the shear strength of the asperities, or the geometry is unfavorable for easy sliding, then the asperities are broken into smaller disaggregated pieces (also known as comminution). This comminution of asperities is also applicable for creep and normal stresses. If the normal stress causing the fracture to mechanically close exceeds the unconfined compressive strength of the asperities, then the contacts between two planes will deform and structurally break. These disaggregated pieces will fill the open space of the fracture (known as the aperture) and hydraulically clog the discrete fracture. Clogging may also result from a colloid mixture of organic material, loose sediments, and groundwater (Bock et al., 2010; Levasseur et al., 2020).

Contrary to clogging or mechanical closure where it is controlled by the mechanical properties of the material, swelling is controlled by the mineralogical properties of argillaceous media and its physicochemical interactions with water. These physicochemical interactions can be categorized into three distinct categories (listed below), all of which result in swelling (Bock et al., 2010).

1. Internal absorption of water into the crystalline structure
2. External water absorption due to negative charges with the clay minerals and positive charges with the silicates
3. Osmotic pressure made by large charge difference between two diffusive layers

Out of these three physicochemical interactions, internal absorption is the more relevant within the confines of this thesis than osmotic pressure or external water absorption. The clay samples that will be characterized and analyzed are Opalinus clay samples, a rock that is composed of smectite minerals (Gaucher et al., 2003). Smectite clay minerals are hydrous minerals that exhibit excellent properties for internal absorption. This is attributed to the non-crystalline lattice structure (relative to silicate minerals) resulting from comparable differences in atomic size of the elements that compose the mineral. These comparable differences leave large openings within the lattice structure and are filled with water molecules (Bock et al., 2010, Levasseur et al., 2020). This results in a volume increase in the clay minerals, that translates macroscopically into swelling of the argillaceous system as a whole. It is important to note that swelling results in fracture closure, but also changes the mechanical properties (e.g., unconfined

compressive strength, ductility, etc.) of the rock. Water intake into the micro-cracks that develop within the elastoplastic deformation of the contact asperities reduce the unconfined compressive strength of the material and disintegrates aggregated elements into smaller elements (Tatone and Grasselli, 2015; Corkum and Martin, 2007).

1.4 Terminology and Morphological Descriptors

The degree of mechanical closure, clogging, or swelling is largely controlled by mechanical and mineralogical material properties, but is also controlled by the surface morphology. The surface morphology are geometric features of rough surface controlling the appearance and structure of the surface; among these features are asperities (i.e. peaks), valleys, and spacings. Asperities are the local maximums of either a surface profile or map, while valleys are the local minimums of the surface. The linear horizontal distance between two asperities or between two valleys is referred to as a spacing. These geometric features are depicted in Figure 2 in red. Within the context of this thesis, surface morphology is treated equivalent to the roughness of the discontinuity. The roughness of surface is made by the macroscopic and microscopic roughness (Figure 2), whose interaction leads to heterogeneous peak and valley spacing throughout the surface. Macroscopic roughness is equated to the morphological information derived from a robust analysis uninfluenced by the asperities and valleys of the surface profile or map, while the opposite is extended to mean the microscopic roughness within this thesis. Both definitions of roughness are relative to the size of the fracture surface and corresponding profile lengths and are applicable within the context of the morphological descriptors and analyses used in this method of characterization. Macroscopic and microscopic roughness are defined under the constraints of asperity and valley influence relative to the sample size, but it is useful to discuss these concepts in the analogy of a generalized wave function. As such, discussion of the Opalinus clay samples and derived results may be discussed in terms used to describe a wave function, namely amplitudes and wavelengths. Amplitude is the vertical separation between the mean line of and the asperities or valleys of a profile, where the mean line is the elevation in a profile where 50% of the area is above and beneath the line. The wavelength is the horizontal separation between two adjacent peaks or between two adjacent valleys.

These morphological surface components can be quantified, and thereby facilitating roughness characterization, by analyzing relevant descriptors of the surface roughness, each pertaining to a component of surface roughness. The descriptors to macroscopic and microscopic roughness are the bearing area curve (BAC), amplitude and amplitude density, respectively. The BAC is a ratio of solid material to ratio of material to air along a horizontal line, known as a bearing line. This bearing line moves vertically along a 2-dimensional surface profile from the absolute maximum to the absolute minimum of that profile (Bhushan, 2000). Resultant curves are 3rd degree polynomial functions, whose slope indicates the distribution of material from the mean line of the profile, a line marking equivalent areas on either side of the line. A steeper and rounder slope of the BAC indicates that material is more vertically distributed, which can be correlated to increased roughness of the surface. An example and more detailed description of the bearing area curve is provided in section 2.1.3. Amplitude and amplitude density are descriptors that complement the BAC descriptor by similarly indicating roughness, but also further identifying local distributions of peaks and valleys in the surface profile or map. In analyzing the amplitude intensity and the distribution (supplemented by amplitude density), the microscopic roughness is indicated. Further information about the amplitude and amplitude density is given in sections 2.1.1 and 2.1.2, respectively.

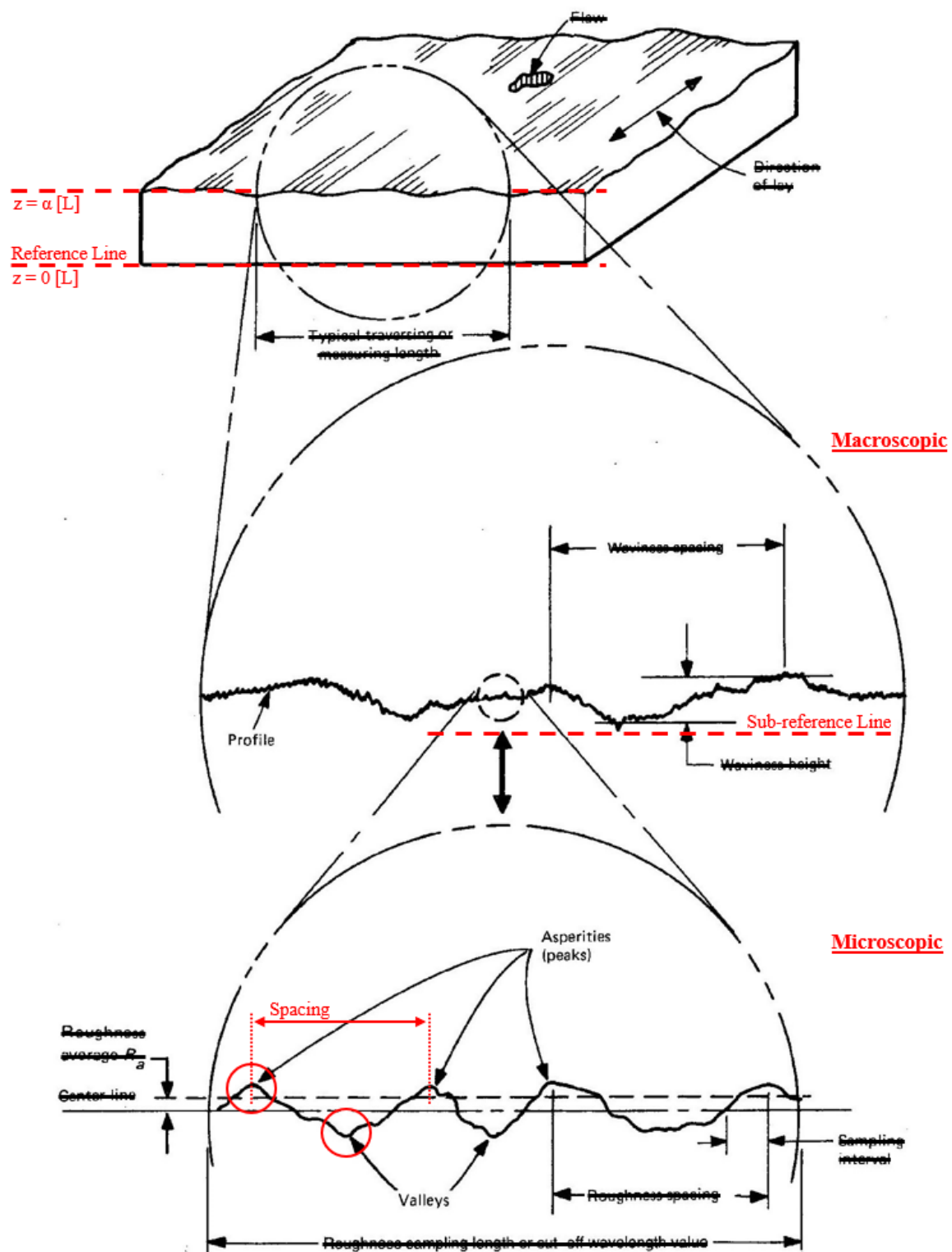


Figure 2: Modified from Bhushan (2000), showing the characteristics of macroscopic and microscopic roughness used within this thesis, as well as the characteristics of morphology used throughout. The macroscopic and microscopic roughness from Bhushan (2000) are represented under the context of wave function characteristics (e.g. wavelength and sampling) and are defined under these conditions. As such, the terminology used by Bhushan (2000) that is irrelevant to the constraints and definitions set within this thesis are crossed out and should be ignored. Definitions used within this thesis are shown in red. The reference line is the reference height from which the heights of the samples are originally measured from and the sub-reference line is the elevation at the absolute minimum of a surface profile.

2 Methodology

Literature (Bhushan, 2000; Pluymakers et al., 2017) shows a spatial analysis of surface morphology, but it is constrained to a singular global value that cannot track local changes in morphology as it relates to swelling. As such, the characterization of the fracture surface, as it pertains to roughness, will not be done using a Fourier analysis to derive a global roughness value from a power spectrum plot, as is done within literature (Bhushan, 2000; Pluymakers et al., 2017). This frequency domain approach is well suited in determining the roughness representative for an entire fracture surface and is not as subject to outlying data; however, it fails to quantitatively show the changes in morphology as determined by the descriptors. As a characterization is to be made for the purpose of quantitatively characterizing fractures subject to interaction with water (and thereby subject to swelling), it is best to characterize the roughness and morphology of the fracture surface with a matrix of data rather than one value. To that end, descriptors will not be analyzed within the frequency-domain, but will remain within the time-domain where amplitudes, amplitude density, bearing area curves, and surface area are locally mapped to quantitatively observe the changes in morphology and subsequent transmissivity in the fracture during experimentation.

Elevation data for two samples of Opalinus clay (Figure 24 in Appendix B), approximately 10mm × 10mm in size, were measured and photographed at the millimeter scale using optical microscopy in order to test the characterization method developed. The data was measured from the $z = 0$ reference line¹ and contained within an .AL3D file which can be opened in Fiji’s ImageJ program and subsequently exported as a delimited tab text image file. This data was obtained via an optical microscope, whose additional functions provided three dimensional pictures of the Opalinus clay samples. The delimited tab text file was then converted into a CSV file and read into Python. In doing so, the elevation data for the rough surfaces of the Opalinus clay samples was put into a matrix, from which descriptors were analyzed. It is important to note that the ‘elevation data’ that is provided and exported into the delimited tab text file are gray scale values and not measured in units of length. This is not a problem with respect to the descriptor analysis (excluding surface area and hydraulic conductivity calculations) as all descriptor spatial analysis is relative to other gray scale values within a matrix or row of the entire dataset. As such, there is no distortion in the analysis of the descriptors or the morphology that can be characterized because of it. The data as well as the dimensions of the sample area must be translated to units of length while calculating for the surface area of the surface. Failing to do so results in unit mismatch between gray scale values and matrix indices, which cannot be used for surface area and hydraulic conductivity calculations.

The descriptors and the characterization that follows is analyzed and considered from a 2-dimensional and 3-dimensional perspective to contrast and determine the limitations and usability of each type of analysis. In comparing analysis results and characterizations in multiple dimensions, the full breadth of the morphological description of the fracture surface is captured. Both types of analysis is achieved using Python coding language. A series of functions is used to create a script capable of finding and quantifying the roughness and transmissivity of the sample from the descriptors of the surface, namely the amplitude, amplitude density, and bearing area curve. The open source JIT compiler Numba is included in the code where possible, making the code more computationally efficient and reducing the run time of the full code for one sample to approximately 30 to 40 minutes. User input is also included within the code, allowing for direct random sampling and coarsening of surface area data. The full code is available on the GitLab repository of the Delft University of Technology [here](#).

2.1 2D Descriptor Analysis

2.1.1 Amplitude

Asperities and valleys are considerable contributors to the morphology and subsequent roughness of the fracture surface. From the amplitude quantification, an indication of the surface roughness is given, particularly as it pertains to microscopic roughness. Encompassed within the breadth of microscopic roughness are asperity contacts and their fluctuation and distribution within the larger macroscopic roughness that is described by discontinuity surface undulation, uninfluenced by peaks and valleys. To

¹Elevation from which all points of the rough surface is measured from. A depiction is shown in Figure 2.

that end, amplitudes are analyzed in 2 dimensions along the x and y-axes of the sample pieces. Surface profiles are reminiscent of wave functions and so the profiles along the x or y-axes were analyzed to identify local peaks and valleys using the *signal.argrelextrema* module from the *SciPy* library. These peaks and valleys were then made relative to the mean line of the profile, as was done by Bhushan (2000), such that all 1st derivative points of inflection (i.e. local max and min) are classified as peaks above the line and as valleys below the line. An example of this reclassification is shown in Figure 3.

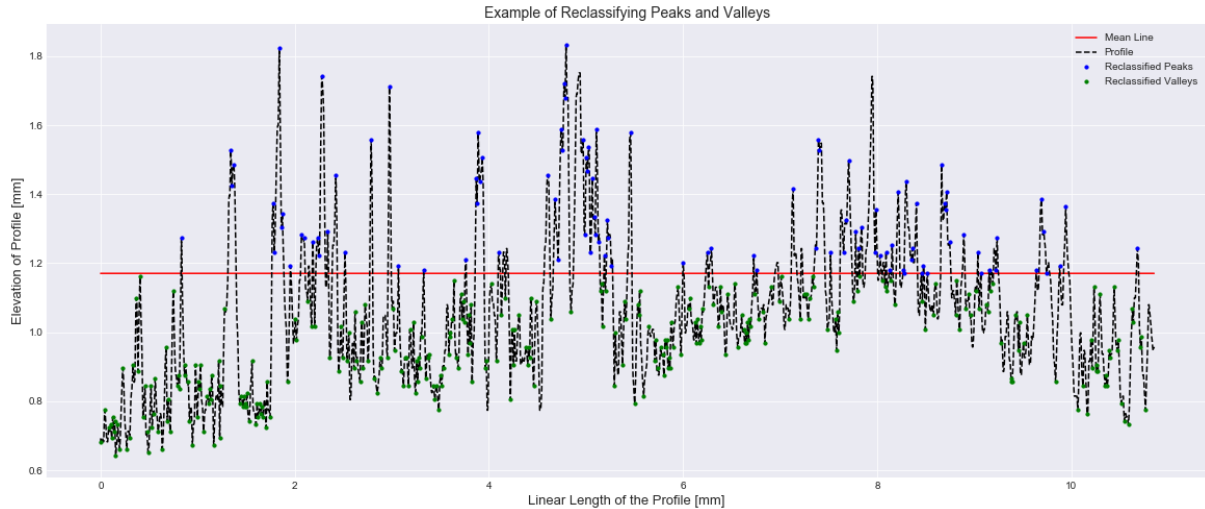


Figure 3: An illustration of the mean line and its use as a boundary between what is classified as areas of depression and elevation in the surface profile. These areas of depression and elevation are dubbed as valleys and peaks, respectively.

The mean line is an imaginary line of each individual profile at a specific elevation z such that the area of the profile underneath the line equals the area above the line. Using the mean line of each profile throughout the matrix to reclassify which maximum and minimums are peaks and valleys further distinguishes depressions and elevations in the sample surface. That being said, peaks and valleys relative to the profile mean line are identified by color-coding and not elevations relative to the mean line (i.e. elevations are kept unchanged). There is a limitation to the accuracy of the code in using the mean line of the profile to reclassify peaks and valleys, namely how accurately the area can be calculated above and below the line at any elevation z .

2.1.2 Amplitude Density

Supplementary to the 2-dimensional amplitude quantification, amplitude density is a further indicator of surface roughness. Amplitude roughness, as it relates to this thesis, refers to the spacing between asperities and between valleys found within a surface profile. This quantifies the proximity of peaks to peaks or valleys to valleys, but is further refined within this thesis toward 'quadrants' of the profile. Amplitude density is useful indicator in quantifying the clustering of peaks throughout the surface, but is inherently subject to spacing between peaks/valleys of non-similar amplitudes. It is superficial to quantify amplitude density between two local peaks/valleys that are significantly different in amplitude and disingenuous to the core purpose of the descriptor. To subvert this, 'quadrants' were made from each profile throughout the matrix to isolate mid-amplitude and high-amplitude ranges of the profile for both valleys and peaks. These valley and peak classifications followed the rules and reasoning given for the 2D analysis of amplitudes; therefore, quadrants below the mean line of each profile were analyzed for valley spacing and quadrants above the mean line were analyzed for peak spacing. Figure 4 illustrates the division of quadrants and classification of quadrants. Local extrema spacing within each of these quadrants were quantified by taking the index position difference between two peaks/valleys within a quadrant and dividing that number by the total number of indices within that specific profile. As such, a dimensionless value is assigned to each peak/valley spacing and is thus applicable to any scale of surface analysis.

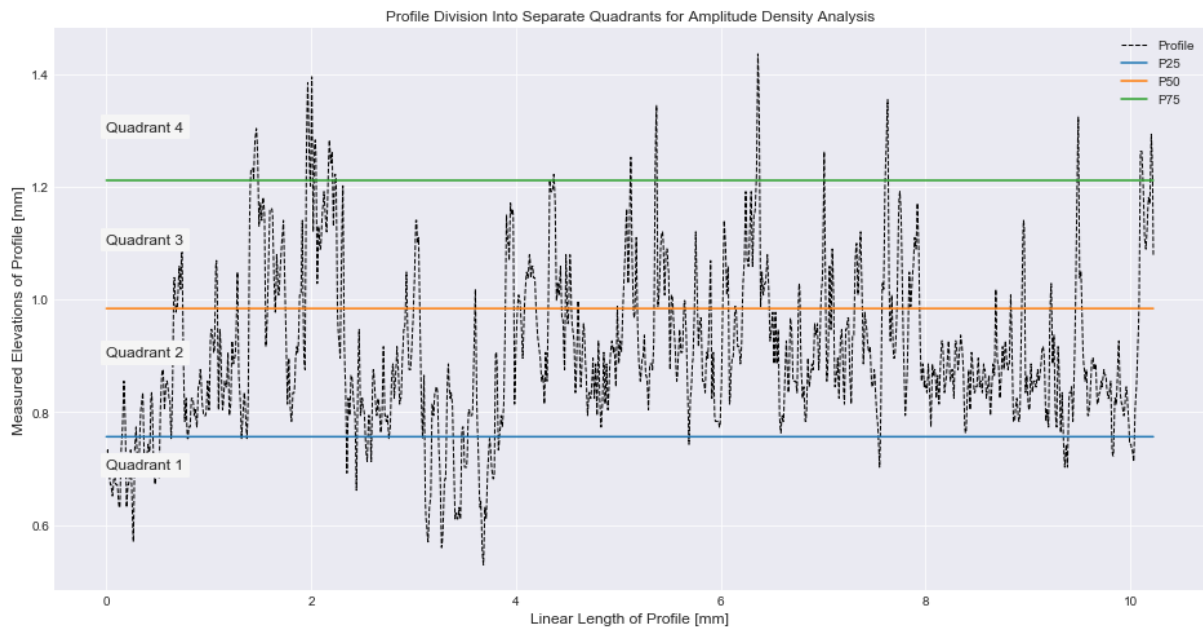


Figure 4: Illustration of quadrant classification and the lines that are used to split the quadrants in each profile. P_i , where i is either 25, 50 or 75, denotes the line of where approximately $i\%$ of the profile area is below the line. This line is calculated using the function `getPercentileArea` and is subject to betterment.

2.1.3 Bearing Area Curve

The bearing area curve (BAC) is a 3rd degree polynomial that represents the amount of material that is above an imaginary line (the bearing line) a distance d above the lowest point in a surface profile. In other words, the slope of the profile is an indicator of the 'waviness' (degree of undulation) of the surface profile. A lower BAC slope is indicative of lower and peaks with longer wavelengths, if the surface profile were to modelled as wave, and thus less 'wavy'. In quantifying the 'waviness' of the fracture surface, the macroscopic roughness is indicated, further contributing to the characterization of the morphology of the surface that is not captured by analyzing amplitude or its spacing. As such, the bearing area curve was calculated for each profile along the x-axis and along the y-axis to capture the full 2-dimensional breadth of waviness as it pertains to the surface. The method used to calculate the BAC by Bhushan (2000) is to calculate the distance between profile-bearing line intersects along the bearing line for rock material (Bhushan, 2000), but this method proves to be computationally inefficient and prone to error. Alternatively, the length ratio value of material along the bearing line is calculated by counting the number of indices of the profile whose corresponding value is above the value of the current bearing line. This process is conceptually identical to the measuring the distance between intersections, but is much more computationally efficient, allowing for faster calculation of the bearing area curves. This process computes over 3000 BACs for the matrix, which are then condensed into singular values for each BAC in order to observe the change in macroscopic roughness throughout the sample area along both the x and y-axis. To condense each bearing area curve into a singular value, the average macroscopic roughness of each BAC is calculated. This is done by fitting a linear line to each profile using the `Polyfit` module in the `NumPy` library and taking the slope of the line as the representative value for average macroscopic roughness. This value is bounded between -1 and 0, where -1 indicates a macroscopic roughness across the sample of uniform wavelength and amplitude and 0 indicates a completely smooth and flat surface. An example is given in Figure 5, showing the line of best fit in red and the bearing area curve in black. For each fitted line of best, the slope of the line was taken and recorded for that profile. Compiling all of these slope values results in two x,y plots that quantifies the variation in macroscopic roughness in both horizontal principal directions. It is important to note that the shape of the bearing area curve, whether it is symmetric or asymmetric, gives an indication as to the local macroscopic roughness throughout the profile. A symmetric bearing area curve indicates homogeneous macroscopic roughness throughout

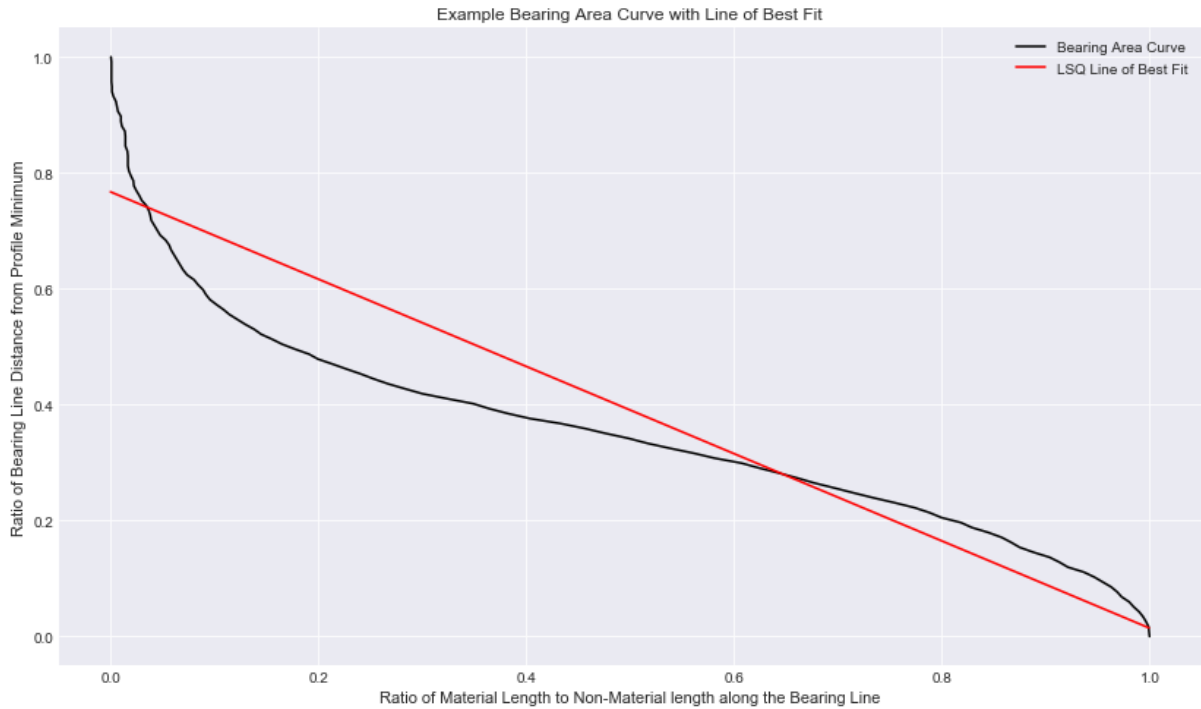


Figure 5: Illustration of Bearing Area Curve with the LSQ line of best fit for the curve. The slope of the fitted line is the singular value used to represent the 2-dimensional Bearing Area Curve.

the profile, but an asymmetric bearing area curve indicates heterogeneity. Figure 5 shows a BAC with asymmetric shape, where the profile from $x = 0.0$ to $x = 0.5$ is steeper and more parabolic than the BAC from $x = 0.5$ onward. This implies that the peaks of the roughness profile are more vertically distributed than the valleys of the profile, which further implies that the peaks are of greater amplitude and thus macroscopic roughness.

2.2 3D Descriptor Analysis

3-dimensional analysis for the amplitudes and bearing area curve is done similarly to their 2-dimensional counterparts. In quantifying the amplitudes from a 3-dimensional perspective, a mean plane was used to separate the valleys and peaks of the surface rather than the mean line of each individual profile. This mean plane is similarly calculated by deriving the elevation z at which the volume above the plane is closest to 50% of the total volume. Volume is treated as the summation of unit columns with an elevation corresponding to that of the relevant datum. The total volume is the sum of all values in the matrix, taking care to subtract all values by the absolute minimum value as this is where the bottom of the value is set. Similarly, a bearing plane was used to calculate the 3-dimensional bearing area curve instead of a bearing line whose values are dependent on the absolute max and min of the profile. The bearing plane is bounded between the absolute extremes of the measured elevations in the dataset, from which the number of points above the current bearing plane is counted. An area of argillaceous material that is below the surface topography is calculated in each slice and is used to make the singular 3D bearing area curve.

2.3 Surface Area

Morphological descriptors facilitate characterizing the roughness of the fracture, but do not fully characterize the fracture as it pertains to swelling. Other driving mechanisms of self-sealing (e.g., mechanical closure via normal stress) are also responsible for the self-sealing phenomenon in argillaceous geomaterials, but are not considered extensively within this thesis. Rather, swelling is mostly considered as it

pertains to the future research of Dr.ir. (Anne-Catherine) A.A.M. Dieudonne and thus is more immediately relevant. To fully characterize the fracture in the context of swelling, the surface area of the rough surface is quantified and visualized at a local scale. Swelling is associated with water intake, which is influenced by the available surface area. The larger the surface area, the larger the water intake, resulting in more swelling. A rough surface of the fracture is contained within an $M \times N$ matrix with uniform cell sizes, which means that, per cell, the surface area of the rough surface is heterogeneous and variable. In quantifying the surface area, swelling observations can be made for any given rough surface in any particular region. With these observations, conclusions can be made regarding the effect of fracture surface morphology on self-sealing within argillaceous material, which contributes towards the larger problem of self-sealing argillaceous geomaterial in radioactive waste repositories.

An accurate surface area calculation of a rough non-geometric surface can be modelled in several ways. One option is to treat each amplitude as a rectangular prism deviating from a mean plane in which the surface area of the rectangular prisms, in conjunction with the planar surface area, equals the total surface area. This is an estimation that provides an upper bound of the surface area given by the measured peaks and valleys. A better estimation, and one that the author has opted for, is to use Delaunay triangulation in combination with Heron's Formula to calculate the triangulated surface area. Using the *Spatial* module within the *SciPy* library, a 3-dimensional triangulation was carried out, from which an object containing the indices of approximately 21×10^6 tetrahedra was generated. An example of such a triangulation is shown below in Figure 6. Each tetrahedron is composed of four indices within the *Simplices* class that directly corresponds to a point within the elevation data. Each amplitude of the sample surface is composed of tetrahedra whose orientation are unknown, which presents two problems in the calculation of the surface area. Tetrahedra are stacked upon on each other with non-regular tetrahedral shapes, thereby presenting only one showing face for the majority of the tetrahedra. Without knowing the specific orientation and knowing for certain which triangle for each tetrahedron is the showing face, two assumptions were made to quantify a surface area estimation. The assumptions are as follows:

1. The showing face will have the highest vertex of the tetrahedron as one of the triangle's points
2. There are no internal tetrahedra within the triangulated sample surface.

That being said, there still lies the choice of which peak-vertex containing face to choose for the surface area calculation. It is unknown which face is the true face, and so an upper bound and lower bound is made by finding the triangles with the highest and lowest surface area of the three triangles. The surface area of each triangle is calculated by using the 3-dimensional distance formula

$$d = \sqrt{(x_1 - x_0)^2 + (y_1 - y_0)^2 + (z_1 - z_0)^2} \quad (1)$$

in combination with Heron's Formula

$$A = \sqrt{s \cdot (s - a)^2 \cdot (s - b)^2 \cdot (s - c)^2}, \quad \text{where } s = \frac{1}{2}(a + b + c) \quad (2)$$

The variables a , b , and c denote the lengths of the three sides of the triangle that is calculated using the points (x_0, y_0, z_0) and (x_1, y_1, z_1) of each edge using equation (1). In finding the highest and lowest surface areas for a singular tetrahedron, the two extreme values are added to separate matrices so that the visualized plots can be compared.

It is important to note that Delaunay Triangulation does result in triangulation between two points in the data that do not reflect the structure of the sample surface. Such an example is shown in Figure 6 with the blue shaded triangle between the absolute maximum and two points at $(0.02, 0, 0.868)$ and $(1.1, 0, 0.885)$. This shaded triangle is one face of a tetrahedron made between two points of data that are not directly connected to each other, and has a surface area that does pertain to the surface of the sample. Faces of these tetrahedra are falsely attributed to the surface area of the rough surface and create a gross over-estimation of the triangulated surface area. As such, a threshold value is used to filter out erroneous and extraneous surface area data. A dynamic threshold is used to filter out this data, whose value is a 10% positive deviation from the median. 10% was chosen as the threshold should be limited to prevent any outlier data from being included, but not too limited so as to exclude relevant data. Additionally, surface area values of zero were also removed from the matrix as this is not possible.

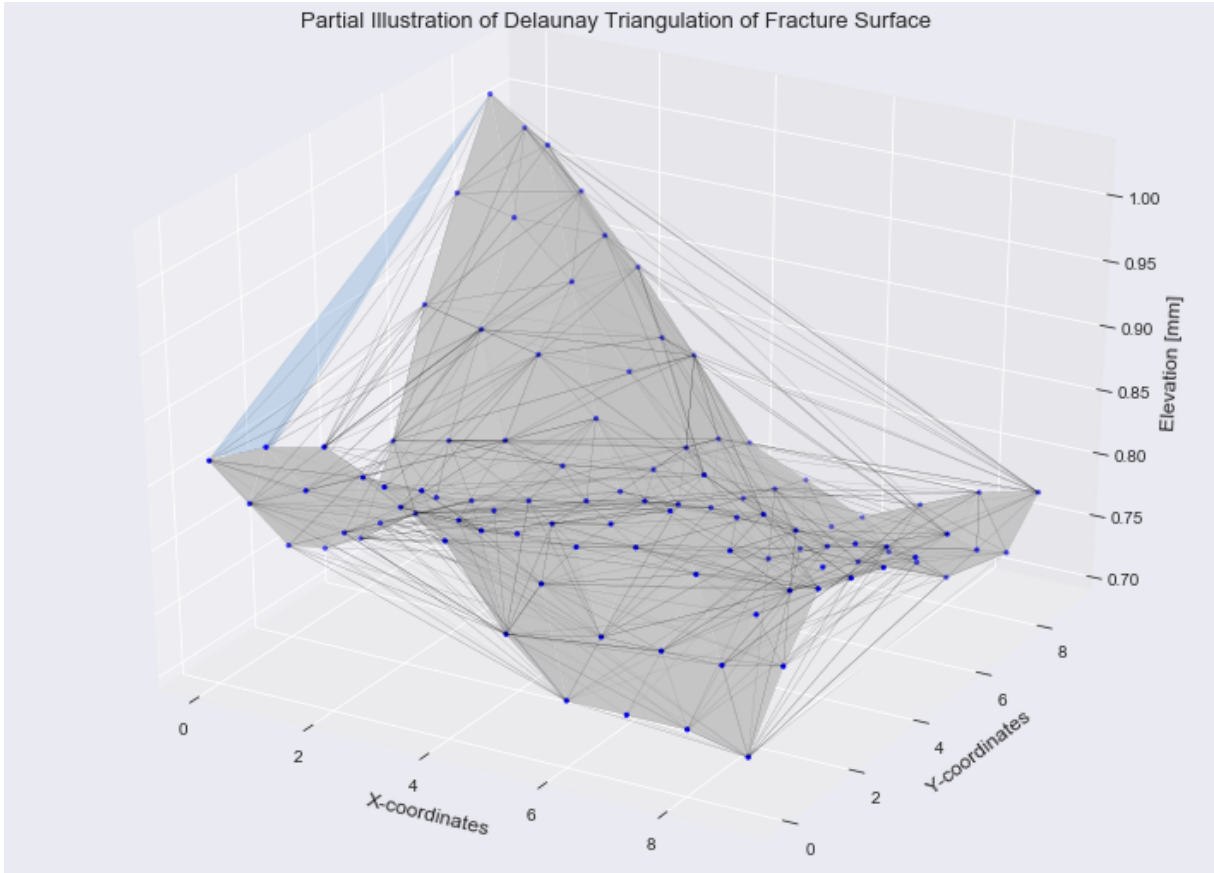


Figure 6: *Delaunay Triangulation of a subset of rough surface data (blue). The local peak in the subset of data is made up of tetrahedra with unknown orientation, but there are also tetrahedra between uncorrelated peaks and valleys (blue triangular face). These tetrahedra erroneously add to the surface area of the fracture surface. The black partially transparent lines are the edges of tetrahedra produced by the Delaunay Triangulation.*

To visualize the surface area quantification, the centroid of each triangle was calculated by taking the mean of (x, y, z) coordinates for all three vertices. Each surface area value corresponds to a tetrahedron that, along with others, belong to one cell of the original matrix data that was triangulated. In other words, one point in the $M \times N$ matrix is made of multiple values of surface area that need to be added and visualized. To do so, the (x, y) centroid coordinates are cast as integers values and all z values of the same (x, y) coordinates are added together and normalized against the planar area of each cell. This normalization creates a dimensionless number that is applicable to any rough surface. It is important to note that as the filtering method is inexact, it is possible for erroneous data to be included into the final surface area data set, which could result in a visualization that is unclear and difficult to interpret. As a compromise, the surface area data was coarsened by adding and homogenizing data across a square grid within the matrix. The resultant coarsened matrix is of similar size to the original $M \times N$ matrix and shows more clearly the behavior and distribution of surface area throughout the surface sample.

2.4 Hydraulic Conductivity

To quantify the amount of self-sealing that occurs within an argillaceous material undergoing swelling, it is necessary to calculate the hydraulic conductivity k of the fracture at any point to measure how much flow is still able to go through the fracture. Literature regarding quantifying permeability as affected by rough discontinuity surfaces are mostly done using flow logs as it is direct measurement of flow passing through the fracture (Zou, 2020; Patterson et al., 2020). This is no suitable means of measurement for this thesis as quantified characterization of transmissivity is done in relation to the morphological

descriptors. As such, the transmissivity is calculated using equation (3)

$$k = \frac{g}{12\nu} \left(\frac{E^4}{JRC^5} \right) \cdot 10^{-12} \text{ m/s} \quad (3)$$

where g is the acceleration due to gravity [m/s^2], JRC is the joint roughness coefficient [-], ν is kinematic viscosity of water at 20°C [m^2/s], and E is the physical aperture within the fracture [μm]. The physical aperture E is related a similar term called the hydraulic aperture e , which is an idealized theoretical aperture for a parallel smooth plated analogy that is completely filled with a laminar flow and is shown in Figure 26 in Appendix B (Barton, 1982; Barton et al., 1985; Barton and de Quadros, 1997; Zambrano et al., 2019). This relationship is given in equation (4) and Figure 26 in Appendix B.

$$e = \frac{JRC^{2.5}}{(E/e)^2} \mu\text{m} \quad (4)$$

Equation (3) is derived from the basic Cubic Law for flow within a parallel plate conduit with planar laminar flow (Barton and de Quadros, 1997; Zambrano et al., 2019). As the hydraulic conductivity to be calculated is meant for induced fractures with matching and potentially interlocking (i.e. correlated) surfaces, the fracture for the Opalinus clay samples are modelled as two matching surfaces separated by 5 μm with the top face showing a slight linear trend and normalized random deviation. Additionally, the in the JRC is introduced and related to e and E (Barton and de Quadros, 1997). This is done to introduce the deviation in flow from the theoretical parallel laminar flow due to roughness of the fracture surfaces (Barton and de Quadros, 1997). Barton and Choubey (1977) and Morelli (2013) note within their literature that the JRC value is originally meant to characterize discontinuity based on the roughness profiles for discontinuities from 10 cm to 1 m, but the Opalinus clay samples analyzed and characterized within this thesis have linear profile length of approximately 10 mm. To ensure that the hydraulic conductivity quantification is conceptually correct, functionality was built to scale sample profiles to 10 cm by coarsening the data. Using the unique index-to-millimeter conversion factors, the number of data points to be averaged together (γ) into a datum is calculated. The net result is a new profile of size δ that is scaled to 10 centimeters. The scaling conversion is dictated by the following set of equations:

$$\delta = \frac{\alpha - R}{\gamma}, \quad \text{where } \gamma = \frac{(100 \text{ [mm]} - R)}{\beta} \quad \text{and} \quad \beta \text{ [mm]} = \alpha \cdot cv \quad (5)$$

where β is the millimeter length of the sample side, α is the size of the original profile, and R is the division remainder relevant to where the term is found (e.g., R in $\frac{\alpha - R}{\gamma}$ is the remainder of $\frac{\alpha}{\gamma}$). The scaling approach does not guarantee that the new profile size will be 10 cm, but rather scales it as close as possible to 10 cm and is assumed to conceptually satisfy the conditions for the JRC. To determine the joint roughness coefficient for a rough surface, a field-derived relationship is used, which is shown in Figure 25 (Barton, 1982; Morelli, 2013) in Appendix B and given in equation (6) (Barton et al., 1985; Barton and de Quadros, 1997; Morelli, 2013).

$$JRC = 400 \frac{a_{max}}{L}, \quad \text{where } L = 10\text{cm} \quad (6)$$

The JRC is a descriptor of roughness for discontinuity surfaces and so the max amplitude a_{max} used is an average value across all profiles in a particular direction (i.e. either along the x or y-axis).

With the above described methodology, a discrete fracture is characterized in terms of both hydraulic conductivity and roughness within the context of self-sealing via swelling. This method of characterization provides a means to record the heterogeneous changes in fracture surface morphology due to water interaction with the argillaceous geomaterial, which in turn facilitates research into self-sealing via swelling and its potential correlation to the initial morphology of an induced fracture.

3 Results

Using the methodology described, two samples of Opalinus clay were analyzed and used to characterize the morphological traits of the sample surface, surface area, and hydraulic conductivity of the modelled fracture. The quantified results and interpretations derived from these results are treated as a proof of concept for the developed fracture characterization method and will act as a conduit to later discussion concerning the method itself. Section 3.1 analyzes the quantified descriptors of amplitude, amplitude density, and bearing area curves (BAC) as they pertain to microscopic roughness, spacing, and macroscopic roughness to derive an interpretation of each Opalinus clay sample. Section 3.2 contains the results of the surface area calculations for an upper and lower bound per sample. Section 3.3 contains the quantified characterization of the hydraulic conductivity through the fracture that is modelled as a parallel plate scenario with a smooth and rough surface.

3.1 Interpretation

The roughness of surface is made by the macroscopic roughness, microscopic roughness, and the spacing of peaks and valleys in the surface. Macroscopic roughness is analogous to undulation of a wave function and is the base roughness of a surface that is built upon by microscopic roughness. Maintaining the wave function analogy, this interference of microscopic roughness with the macroscopic roughness (whether it is constructive or destructive) results in attenuated and augmented amplitudes throughout the surface with variable spacing. The spacing between these amplitudes note the density of peaks and valleys within an area and to the heterogeneity of roughness in the surface. As such, the quantitative description detail each of these three components to standardize the surface description and make a means of comparison between different surfaces. To that end, Opalinus clay samples 1 and 2 are described below in sections 3.1.1 and 3.1.2, respectively.

3.1.1 Opalinus Clay Sample 1

The macroscopic roughness of Opalinus clay sample 1 (see Figure 24 (a) for the optical image) is provided by the shape of the profile and the slope value calculated for the fitted line, whose values are bounded between 0 and -1. A slope value of 0 indicates that the surface is completely smooth, while a slope value of -1 indicates that the surface is very rough and completely symmetrical in undulation. The bearing area curve (BAC) derived from a 2-dimensional analysis for sample 1 is given in Figure 7 and displays macroscopic roughness in both directions along the x and y-axes. The BAC is dimensionless in both directions, such that this curve is applicable to any similarly rough surface of any scale. From Figure 7, it is observed that the average slope for BAC along the x-axis is -0.71, while the average slope value along the y-axis is -0.71. Compared to the global slope value obtained from Figure 8 (i.e. -0.61), the macroscopic roughness is higher under 2-dimensional analysis than in the 3-dimensional analysis. The variations seen within Figure 7 shows that roughness along the x-axis does not fluctuate dramatically and stays mostly between -0.78 and -0.68. Variation along the y-axis for slope values is more dramatic, showing a large shift in macroscopic roughness between $y = 2.5\text{mm}$ and $y = 4\text{mm}$ of the bottom plot. The interaction macroscopic roughness along the x and y-axes indicates that a large depression rests with the bottom-left corner of sample, but that the macroscopic roughness throughout the sample is mostly homogeneous. The profile shape of the bearing area curve in Figure 8 indicates that peaks within the sample do have larger amplitudes than the valleys at lower elevation of the material.

Observations from the BAC analysis are corroborated by the amplitudes observed in Figures 9 and 10. Figure 9 shows the color coded amplitudes with respect to the mean line of each profile whose values are the original elevations measured with the optical microscope, while the elevations of Figure 10 are relative to a calculated mean plane.

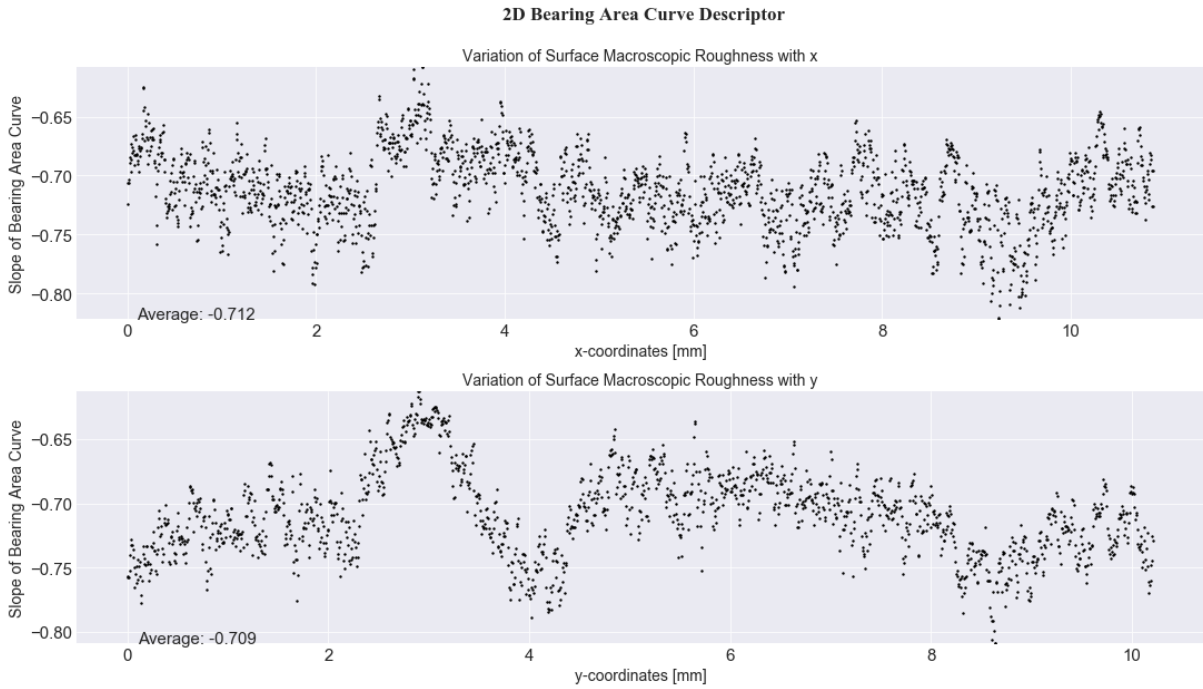


Figure 7: Quantified slope values of fitted lines for sample 1. The top figure shows change along the x-axis, while the bottom figure shows change along the y-axis.

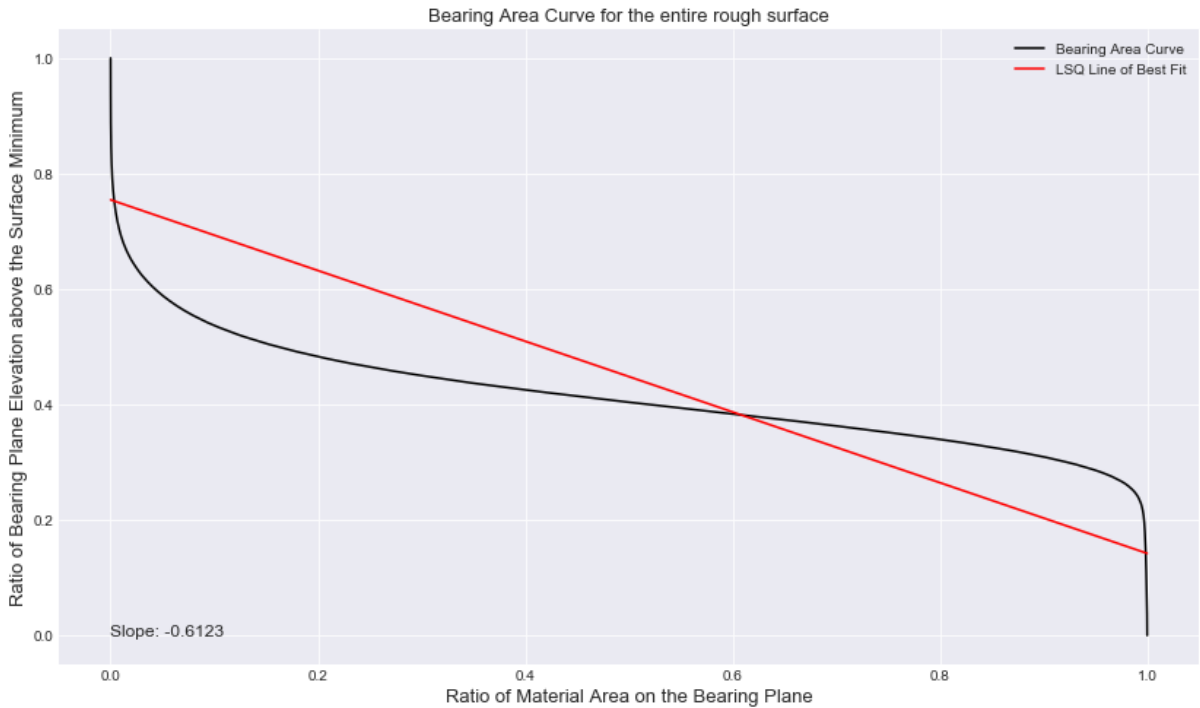


Figure 8: 3-dimensional bearing area curve for Opalinus Clay sample 1 with a moving bearing plane bounded between the absolute maximum and absolute minimum of the surface. The least squares fitted 1st degree polynomial (red) is used to derive a representative slope for the BAC, indicating global surface undulation.

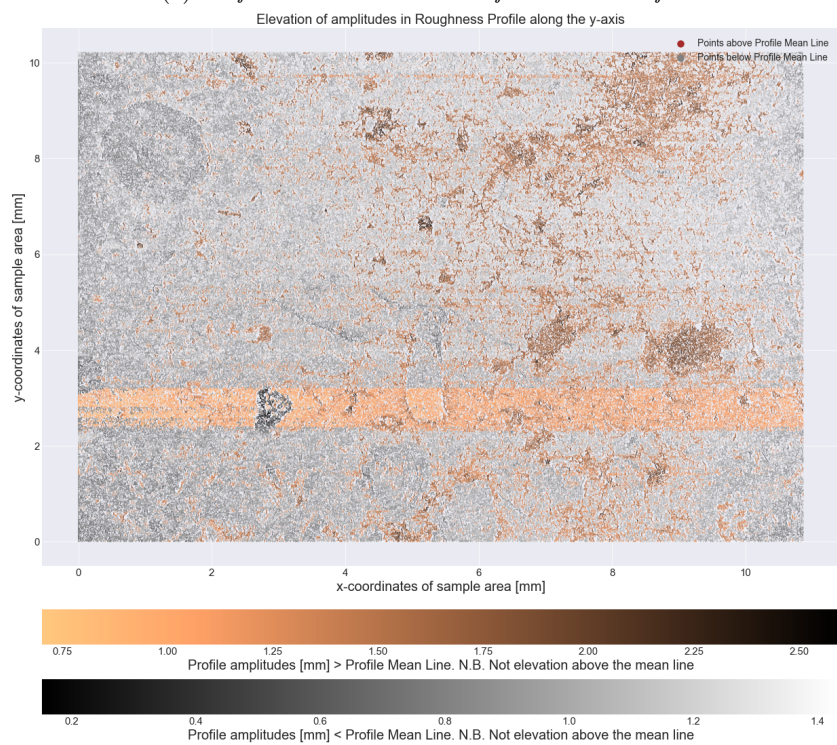
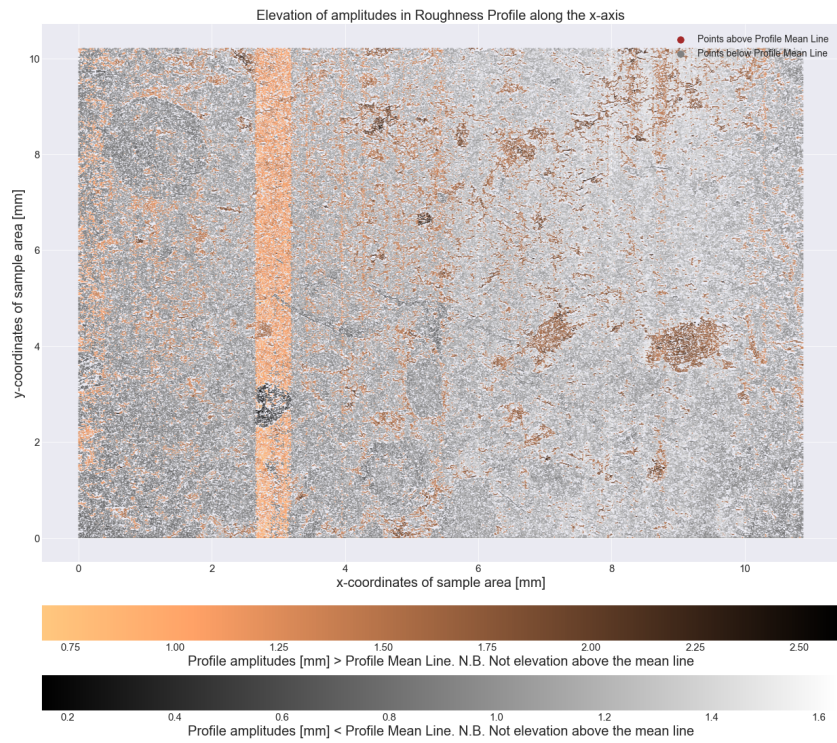


Figure 9: 2D amplitude analysis of *Opalinus* clay sample 1 with peaks and valleys of the surface color coded with respect to the mean line of an individual profile in either the x or y -axis.

There is a depression centered at $(x,y) = (3,3)$ mm as is indicated by the large slope change between $x = 2.5$ mm and $x = 3.5$ mm of bottom plot of Figure 7. The amplitudes are also observed to be intermixed, but generally is divisible into regions where certain amplitudes are more prevalent. Figures 9 and 10 show that the higher amplitudes extend from the upper right corner to the center of the sample area, while deeper valleys are typically located in the left-hand side of the sample area.

While this is the case, Figures 11 and 12 show that higher peaks in the upper-right quadrant are typically spaced 1 - 1.5 mm, while valleys, bounded between $x = 0$ mm and $x = 3$ mm, are typically spaced by 0.1 - 0.5 mm. This is corroborated by Figure 10. This indicates that the microscopic roughness is non-uniformly distributed among the sample, resulting in flatter patches of surface within the center of sample 1 and intermittent rough surfaces towards the right. Microscopic roughness constructively interferes with the macroscopic roughness in the right region of sample 1, but has long wavelengths that result in sparsely distributed peaks. Towards the right, the microscopic roughness also constructively interferes with the macroscopic roughness but has a shorter wavelength that results in a dense region of valleys and peaks. Regions of the sample area between the peaks and valleys are smoother, where the microscopic roughness destructively interferes with the underlying macroscopic roughness. The culmination of these observations is an interpretation that is visualized by Figure 13, showing the approximated regions of roughness for high amplitude peaks (red) and valleys (blue) and an approximation of the microscopic roughness expressed as a wave function.

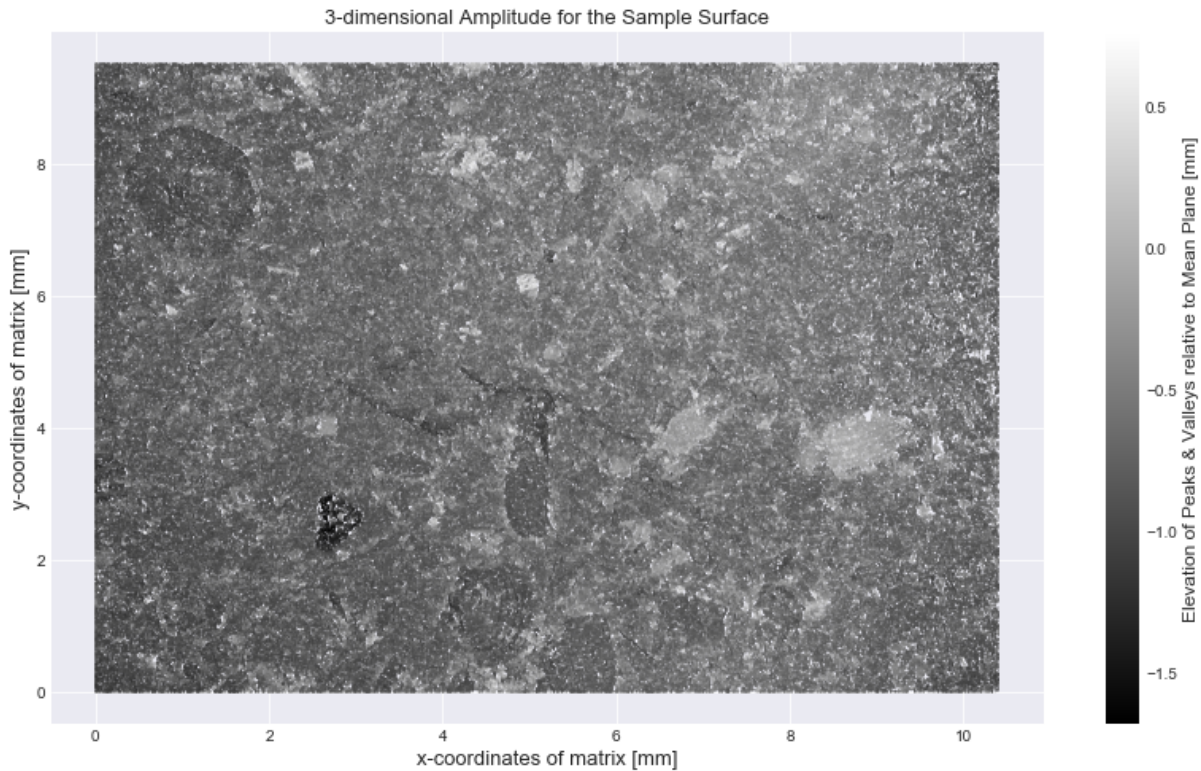


Figure 10: 3-dimensional visualized amplitudes for *Opalinus* clay sample 1 with elevations relative to a mean plane calculated by the function `getPercentileZ`.

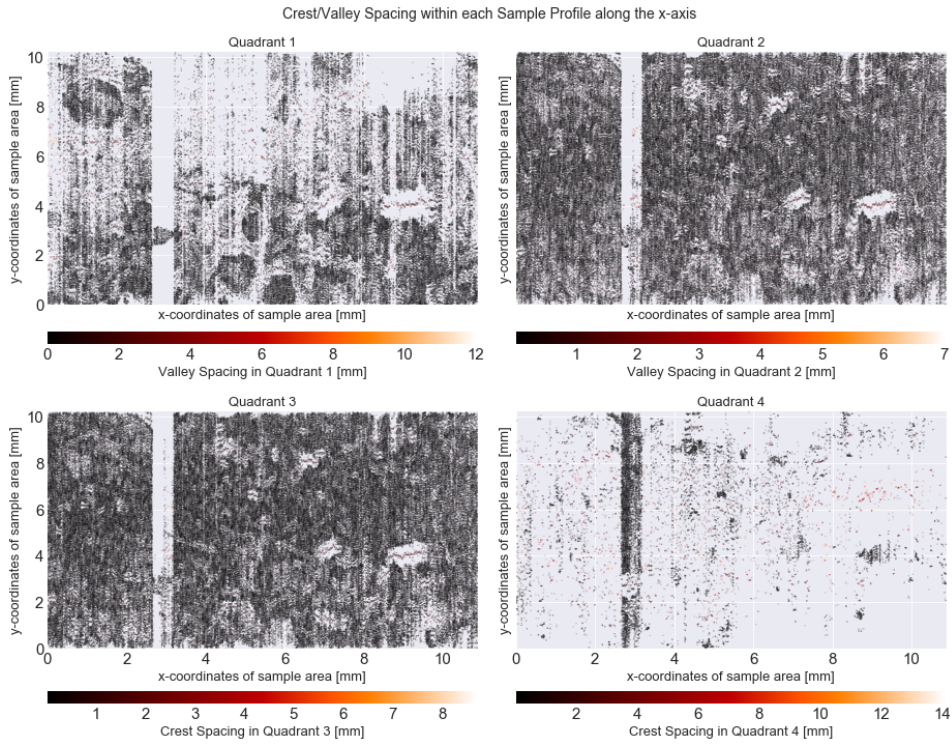


Figure 11: *Sample 1 x-axis profile: Valley spacing within quadrants 1 and 2 (top row) and peak spacing within quadrants 3 and 4 for profiles in the x-axis for sample 1.*

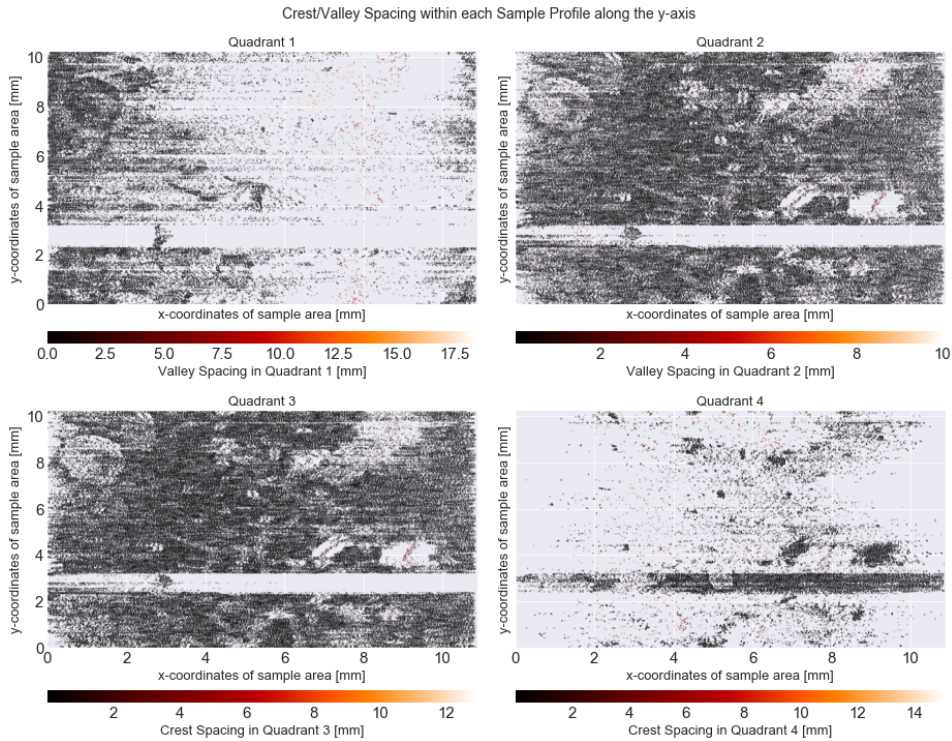


Figure 12: *Sample 1 y-axis profile: Valley spacing within quadrants 1 and 2 (top row) and peak spacing within quadrants 3 and 4 for profiles in the y-axis.*

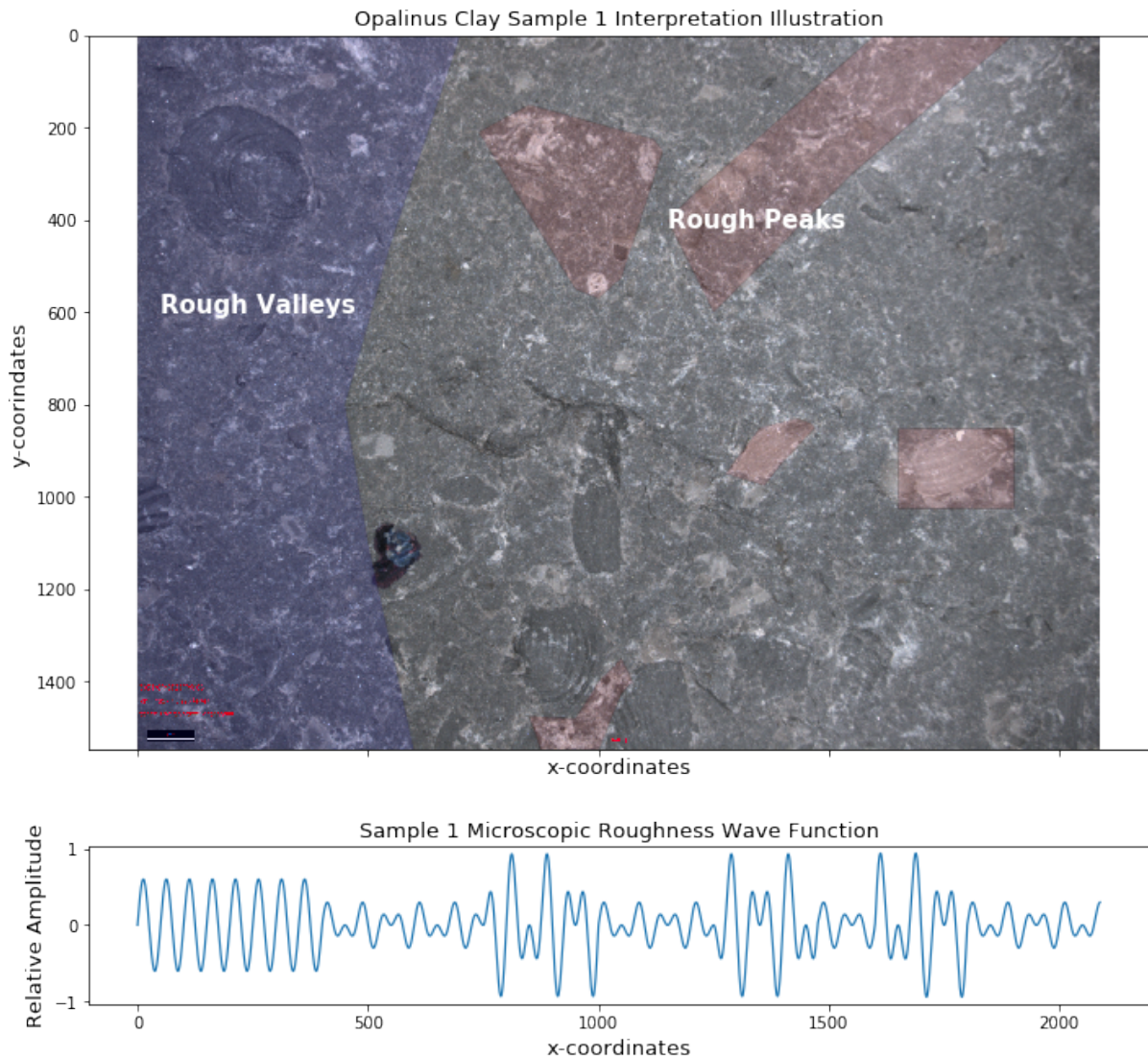


Figure 13: A visualization of the division of roughness within sample 1, showing the regions of high amplitude roughness in red and blue and regions. The negative space between the red and blue polygons is the lower amplitude roughness of the sample that is smoother than the two highlighted regions. The approximated wave function for microscopic roughness is the general function for roughness along the x-axis.

3.1.2 Opalinus Clay Sample 2

The macroscopic roughness of Opalinus clay sample 2 (Figure 24 (b)) is given by the shape of the profile for the 3-dimensional bearing area curve (Figure 15) and the slope values that are bounded between 0 and -1. Figure 14 shows that there is a trend of increasing roughness with increasing x and increasing y. The slope at $x = 0\text{mm}$ is approximately -0.68 and decreases to a slope value of -0.88 at $x = 7.6\text{mm}$. The slope at $y = 0\text{mm}$ is approximately -0.8 and decreases to -0.9 at $y = 8.2\text{mm}$, but does not do so linearly. Fluctuations in the macroscopic roughness along both the x and y-axes show, that there are regions in sample 2 which are either smoother or rougher. Between $y = 1\text{mm}$ and $y = 2\text{mm}$ and between $x = 1.5\text{mm}$ and $x = 2.5\text{mm}$ there is increase in the slope to approximately -0.65, which indicates that the surface is macroscopically smoother than the surrounding area. As such, the data indicates that sample is increasingly rough from the bottom-left corner to the upper-right quadrant. Figure 15 corroborates this local heterogeneity, as is indicated by the slope of the profile. The slope of the profile between $x = 0$ and $x = 0.5$ is considerably steeper and smoother than the profile between $x = 0.6$ and $x = 1.0$,

indicating that the peaks have much higher amplitudes than those of the peaks at lower elevations. In other words, the profile shape indicates that the macroscopic roughness of the sample is greater than the global average where the highest peaks are located.

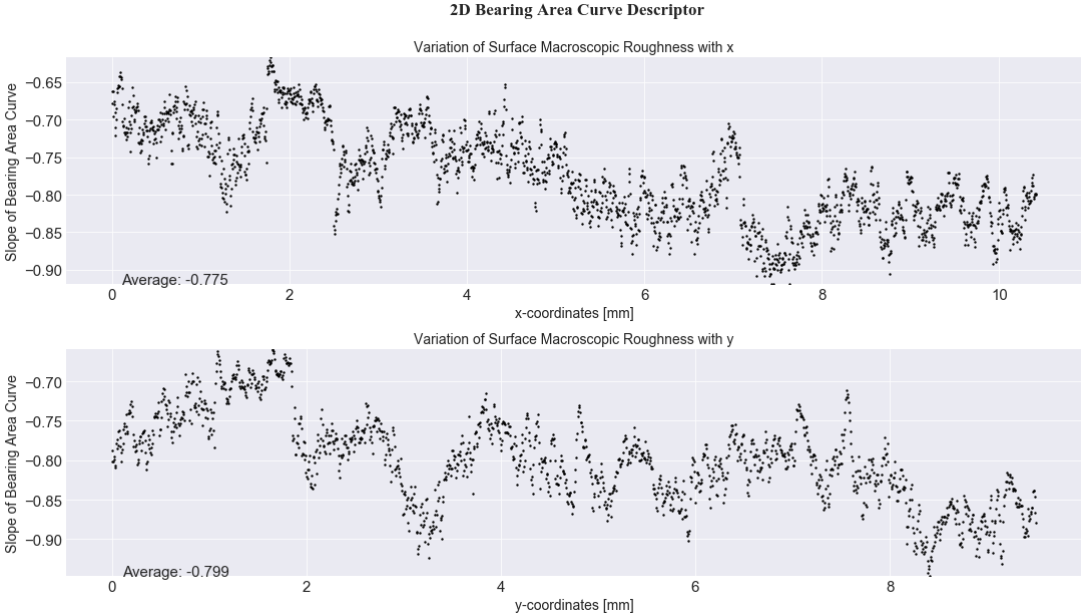


Figure 14: Quantified slope values of fitted lines for sample 2 that are illustrated as points within an x,y -plot. The top figure shows change along the x -axis, while the bottom figure shows change along the y -axis.

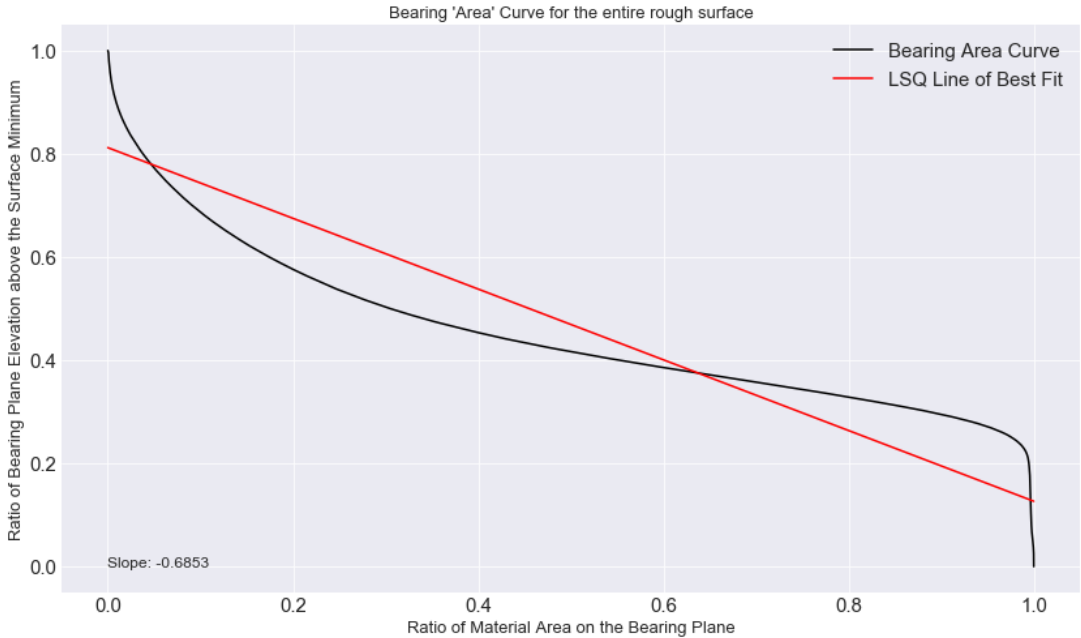
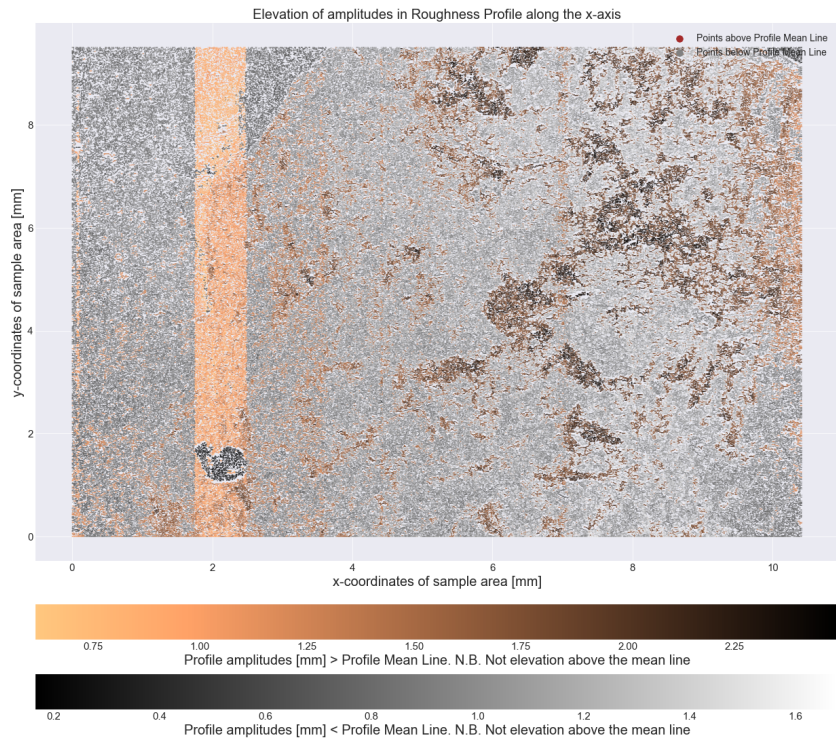
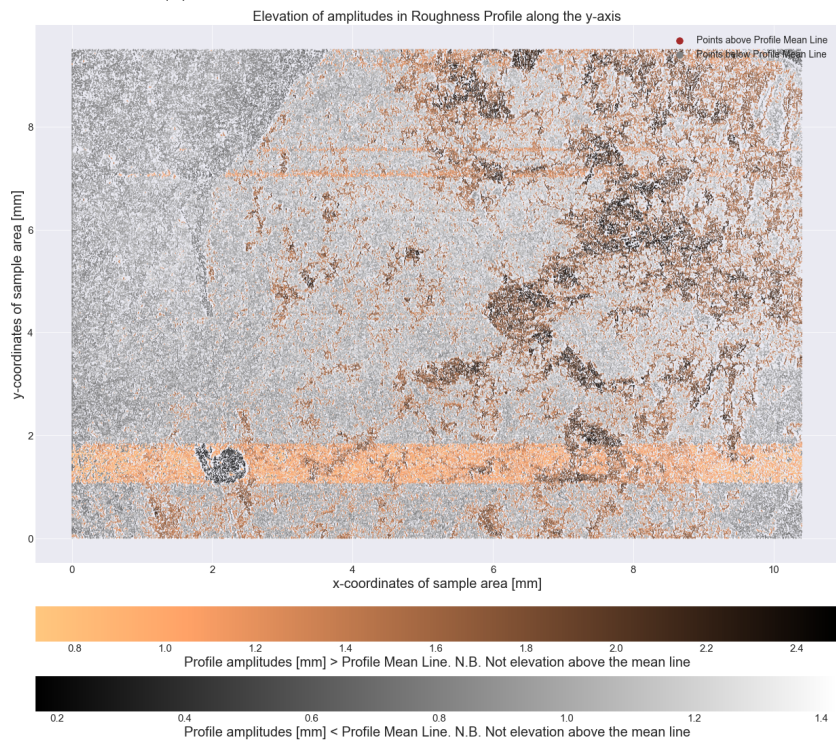


Figure 15: 3-dimensional bearing area curve for *Opalinus Clay* sample 2 with a moving bearing plane bounded between the absolute maximum and absolute minimum of the surface. The least squares fitted 1st degree polynomial (red) is used to derive a representative slope for the BAC, indicating global surface undulation.

The observations from the bearing area curve are corroborated by the amplitudes observed in Figures 16 and 17.



(a) Profiles taken in the x-axis for all values of x .



(b) Profiles taken in the y-axis for all values of y .

Figure 16: 2D amplitude analysis of *Opalinus* clay sample 2 with peaks and valleys of the surface color coded with respect to the mean line of an individual profile in either the x or y -axis.

Figure 16 shows the color coded amplitudes with respect to the mean line of each profile whose values are the original elevations measured with the optical microscope, while the elevations of Figure 17 are relative to a calculated mean plane. The mean plane calculated is unique for each sample surface is calculated for the z value that is closest to having 50% volume below and above the plane at that particular z . The mean plane elevation is completely uniform and has no dipping directions.

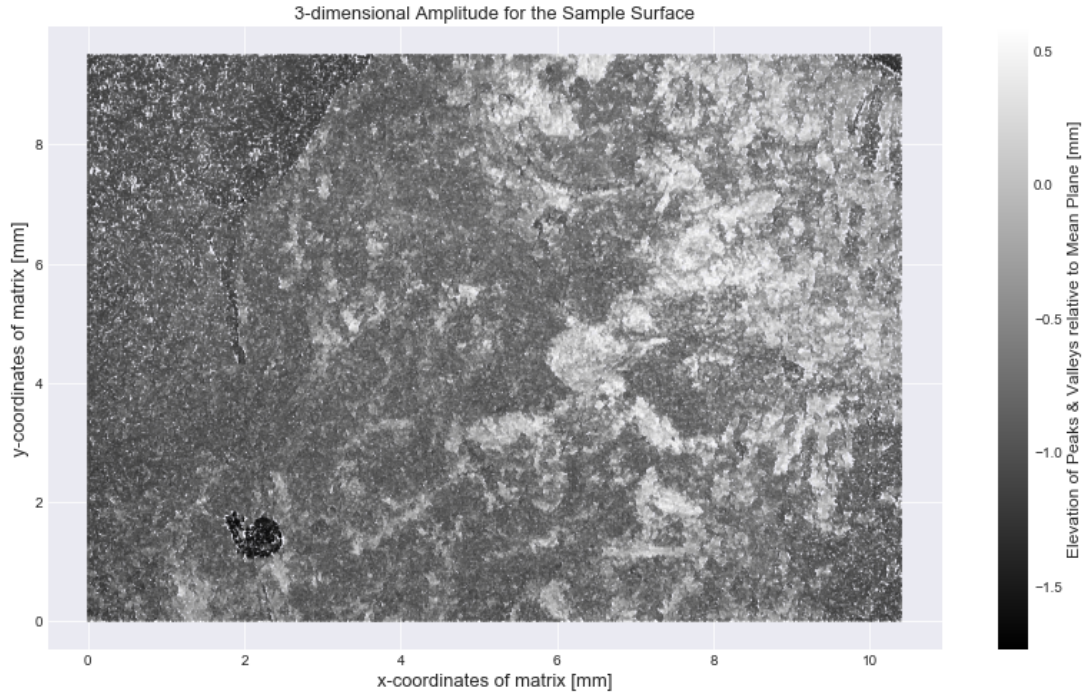


Figure 17: 3-dimensional visualized amplitudes for *Opalinus* clay sample 1 with elevations relative to a mean plane calculated by the function `getPercentileZ`.

High peaks with elevations of 2.2mm to 2.35mm are located within the upper-right quadrant of the sample surface between $x = 6\text{mm}$ and $x = 10.2\text{mm}$, while lower elevations with approximate values of 0.4 mm are located in the left and bottom-right margins of the sample. The left margin encompasses the sample surface below $x = 2.5\text{mm}$ approximately, while the right margin is the bottom-right corner of the sample area, bounded between $x = 9\text{mm}$ and $y = 3.5\text{mm}$. Within these regions, the spacing between valleys is short and is typically less than 0.1mm, as is indicated by Figures 18 and 19. These amplitude density figures show the amplitude density for mid and high range peaks and valleys for the profiles in both the x and y -axes and is quantified by a ratio of the spacing distance to the total profile length. As such, each quadrant shows the relative spacing and clustering of peaks and valleys of various amplitudes and their location on the sample surface, indicating both the wavelength and amplitude of a microscopic roughness wave function. Quadrant 1 of Figures 18 and 19 show the left marginal and bottom-right regions (i.e. $x \leq 2.5\text{mm}$ & $x \geq 9\text{mm}$) to be densely spaced valleys with amplitudes ranging between 0.8mm and 1.3mm, and bordering a region of smoother surface (i.e. lower amplitude). Between $x = 2.5\text{mm}$ and $x = 6\text{mm}$, the amplitudes are lower than the adjacent regions (i.e. $x < 2.5\text{mm}$ and $x > 6\text{mm}$), indicating the microscopic roughness is destructively interfering with the underlying macroscopic roughness. Figures 18 and 19 show that the spacing between both peaks and valleys is lower than 0.1mm within the center of the sample area, but increases to 1 - 2mm for $x > 8\text{mm}$. The microscopic roughness, as is indicated by the data, can be construed as a wave function with constructively interfering amplitudes with a short wavelength that becomes shallower and wider (i.e. longer wavelength) for several millimeters and reverts back to previous behavior for 2 millimeters, albeit with a larger amplitude. The culmination of these observations is an interpretation that is visualized by Figure 13, showing the approximated regions of roughness for high amplitude peaks (red) and valleys (blue) and an approximation of the microscopic roughness expressed as a wave function.

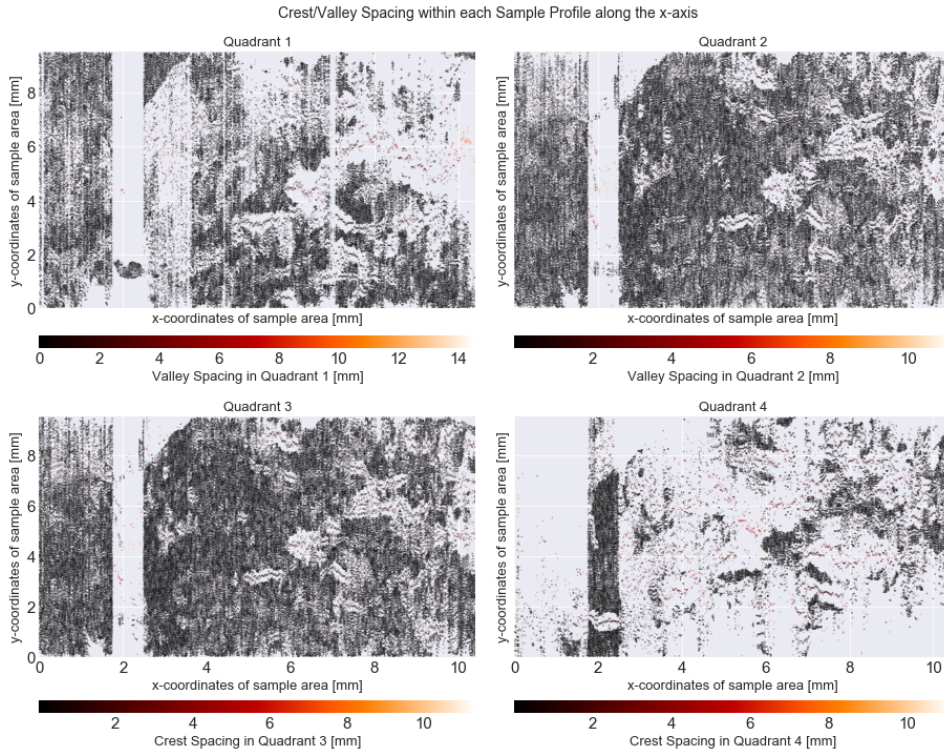


Figure 18: *Sample 2 x-axis profile: Valley spacing within quadrants 1 and 2 (top row) and peak spacing within quadrants 3 and 4 for profiles in the x-axis for sample 1.*

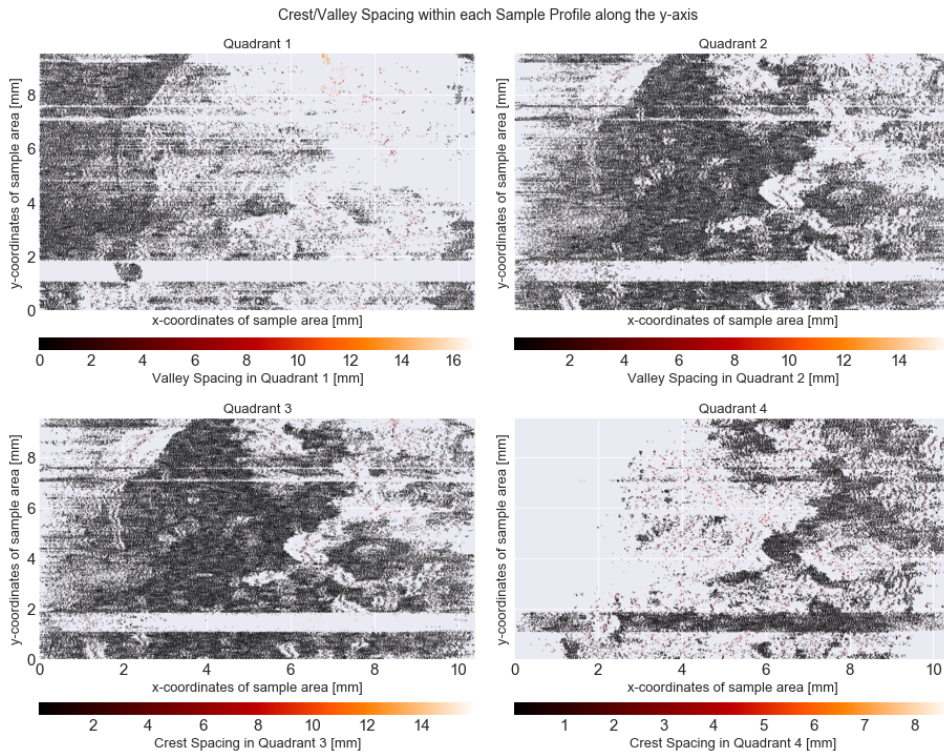


Figure 19: *Sample 2 y-axis profile: Valley spacing within quadrants 1 and 2 (top row) and peak spacing within quadrants 3 and 4 for profiles in the y-axis.*

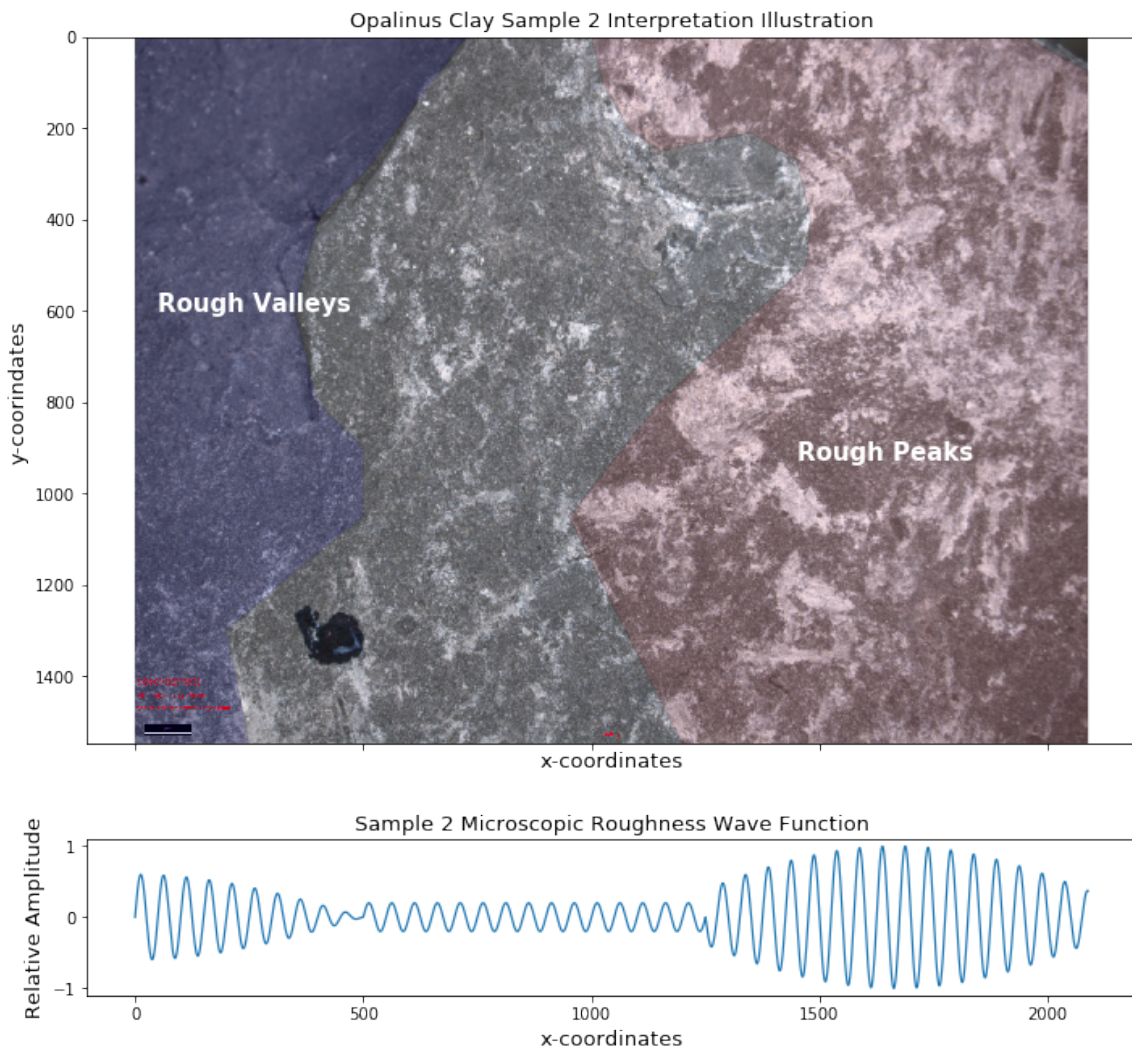
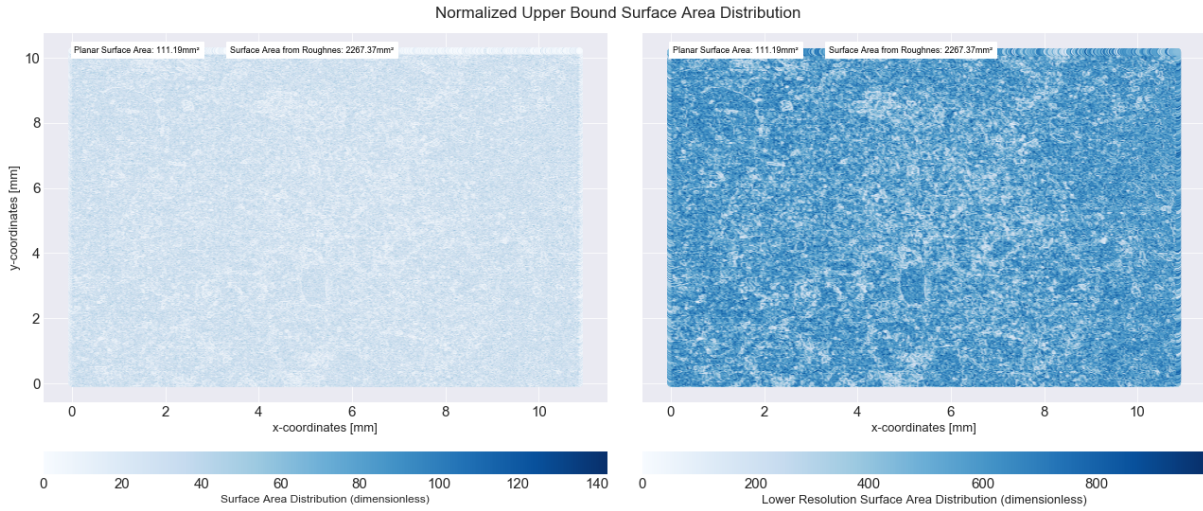


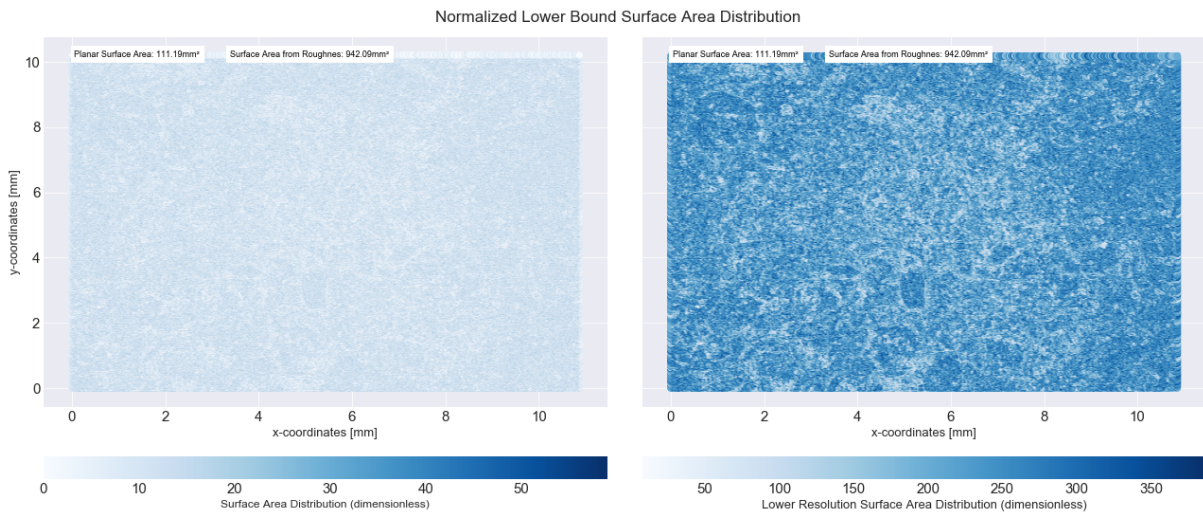
Figure 20: A visualization of the division of roughness within sample 1, showing the regions of high amplitude roughness in red and blue and regions. The negative space between the red and blue polygons is the lower amplitude roughness of the sample that is smoother than the two highlighted regions. The approximated wave function for microscopic roughness is the general function for roughness along the x-axis.

3.2 Surface Area

Figure 21 shows the lower (bottom row) and upper bound (top row) of the surface area calculations for sample 1. For a sample area of interest of 10.88 mm by 10.22 mm, the planar surface area of sample 1 is 111.19 mm². The estimated range of surface area for the triangulated rough surface is bounded by the quantified upper and lower surface area bounds, with values of 2267.37 mm² and 942.09 mm².



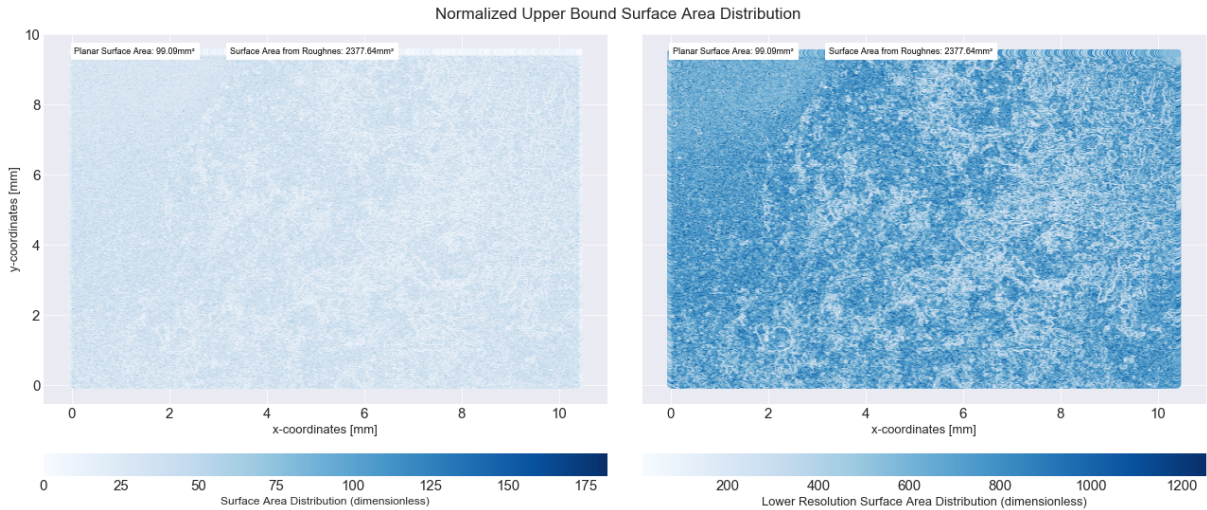
(a) Upper bound calculated by taking the maximum surface area of the triangles associated to the vertex with the highest elevation.



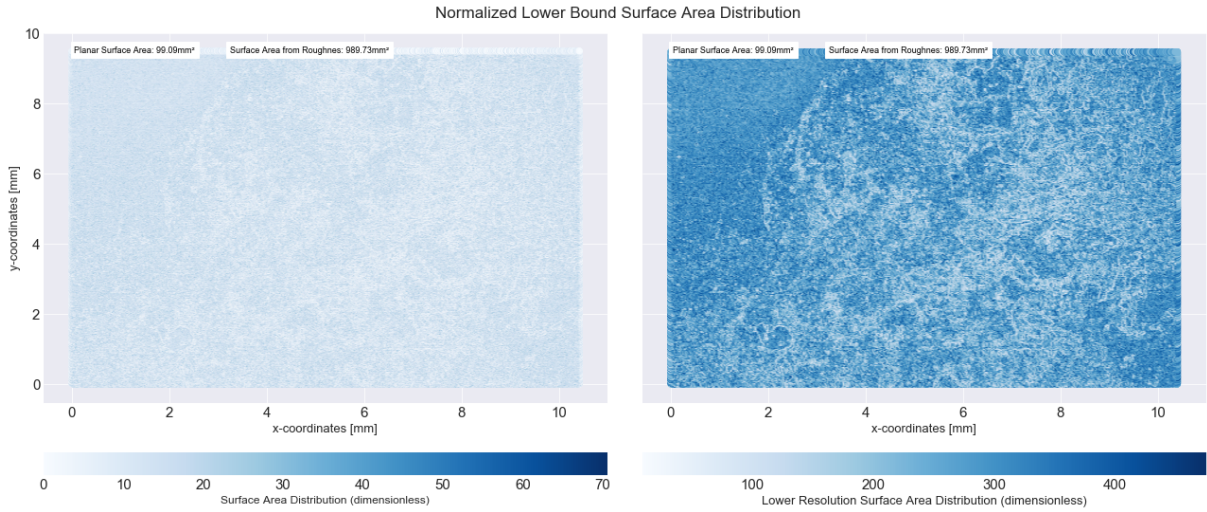
(b) Lower bound calculated by taking the minimum surface area of the triangles associated to the vertex with the highest elevation.

Figure 21: Triangulated surface area for the rough surface of sample 1 and visualized by normal (left) and reduced (right) resolution. Data was coarsened using a 5x5 square grid within the matrix and adding all values encompassed within the grid.

Figure 22 shows the lower (bottom row) and upper bound (top row) of the surface area calculations for sample 2. For a sample area of interest of 10.42 mm by 9.51 mm, the planar surface area of sample 2 is 99.09 mm². The estimated range of surface area for the triangulated rough surface is bounded by the quantified upper and lower surface area bounds, with values of 2377.64 mm² and 989.73 mm².



(a) Upper bound calculated by taking the maximum surface area of the triangles associated to the vertex with the highest elevation.



(b) Lower bound calculated by taking the minimum surface area of the triangles associated to the vertex with the highest elevation.

Figure 22: Triangulated surface area for the rough surface of sample 2 and visualized by normal (left) and reduced (right) resolution. Data was coarsened using a 5x5 square grid within the matrix and adding all values encompassed within the grid.

3.3 Hydraulic Conductivity

A correlated fracture model was used to calculate the hydraulic conductivities along the x and y-axes, giving k_x and k_y . The physical aperture of the modelled fracture for OPA samples 1 and 2 is $5\mu m$ is chosen to be within the expected range of physical aperture that would occur in the field. The joint roughness coefficient is calculated along both axes (i.e. x and y) of each sample as the hydraulic conductivity is dependent upon the surface roughness encountered along the linear length of flow, and so L and a_{max} will also be variable. As the roughness is typically anisotropic for a fracture surface, it is expected that the hydraulic conductivity will also be anisotropic. The hydraulic conductivities for sample 1 is: $k_x = 1.78 \times 10^{-7}$ m/s and $k_y = 7.75 \times 10^{-7}$ m/s. The hydraulic conductivities for sample 2 is: $k_x = 8.01 \times 10^{-9}$ m/s and $k_y = 2.10 \times 10^{-7}$ m/s. The typical hydraulic conductivity of the OPA for the samples is 2×10^{-13} m/s.

4 Discussion

Having shown that the developed method of quantitative characterization through morphological descriptors is operational and produces data of reasonable expectations that can be interpreted, it is important to discuss the method itself as the method is the contribution being made to the further understanding of self-sealing within argillaceous material. The interpretation of data resulting from the method presented within this thesis is a proof of concept and acts as a conduit for discussion surrounding the method. To that end, a self-assessment is made regarding uncertainties and limitations of the method as well as improvements that are to be made for future use. Sections 4.1 and 4.2 discusses uncertainties as it relates to hydraulic conductivity and surface area quantification, respectively. Section 4.3 discusses the goal of capturing the full breadth of data possible from the descriptors and the relevancy of 2-dimensional and 3-dimensional analysis to that goal. Section 4.4 discusses possible developments that can be made in order to improve the method as it relates to machine interpretation and larger data sets.

4.1 Uncertainties in hydraulic conductivity

The foundation of the method used to quantify the hydraulic conductivity (aka permeability as it is denoted within the literature) is the adjustment of the Cubic Flow Law (3) for laminar flow within a parallel smooth faced planar conduit. This conduit is adjusted for drag forces enacted on it by the rough morphology of the surface. For fracture flow analysis using correlated surfaces, as is done within this thesis, the drag forces are introduced with the empirically derived relationship observed by the figure (Figure 26) given by Barton et al. (1985) and Barton (1982) and is expressed as (4) (Barton, 1982; Barton et al., 1985; Barton and de Quadros, 1997; Zambrano et al., 2019). It is stated within the literature of Barton and de Quadros (1997) and Barton et al. (1985) that both E and e are expressed in units of micrometers, meaning that the units of the relationship are heterogeneous² (i.e. the units do not match on either side of the equivalency sign). To check for the validity of the relationship defined by Barton et al. (1985), the empirical data from Figure 26, used by Barton et al. (1985) were plotted and compared to the original relationship for differing values of JRC , as given by Figure 23.

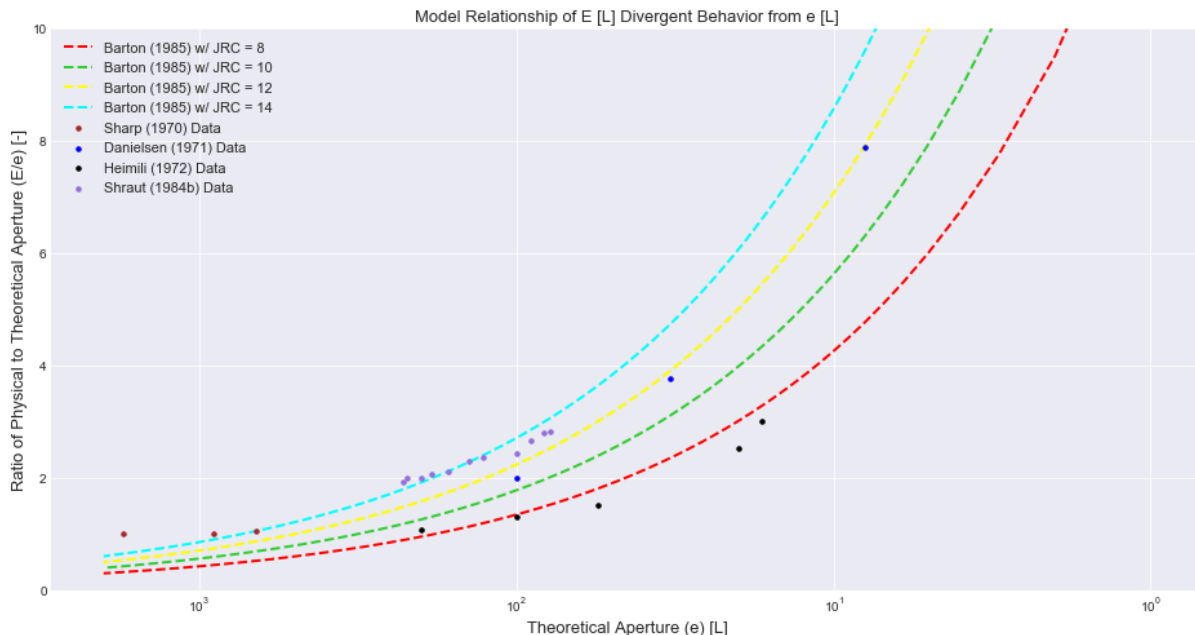


Figure 23: Deviation in real aperture E from the theoretical aperture e for decreasing e modelled by equation (4), and is plotted against the data used by Barton et al. (1985) for experiments conducted by Sharp (1970) (brown), Danielsen (1971) (blue), Heimli (1972) (black), Schrauf (1984) (purple).

²Isolating e within equation (4), which is unitless, leads to equation $e = E^2/JRC^{2.5}$ where e has units of μm^2 .

The divergent behavior of equation (4) suitably follows the divergent behavior of the empirical data from the experiments of Sharp (1970), Danielsen (1971), Heimli (1972), Schrauf (1984), and as such, is used in the calculation of hydraulic conductivity despite the unit heterogeneity. e within the Cubic Law is substituted by $E^2/JRC^{2.5}$, giving

$$k = \frac{g}{12\nu} \left[\frac{E^2}{JRC^{2.5}} \right]^2 = \frac{g}{12\nu} \frac{E^4}{JRC^5} \quad (7)$$

The literature states that $E^2/JRC^{2.5}$ has units of L^2 , thereby giving units of $\frac{L}{s}$ for the calculated permeability. If one goes by the original definition of physical aperture (i.e. units of L), then a unit analysis shows that e^2 is equal to L^4 , thereby giving units of $\frac{L^3}{s}$ for k . Units of $\frac{L^3}{s}$ present a volume discharge and may be plausible when the fracture is considered as a discrete system consisting of unit columns with a height E . When the fracture is considered as such, the k calculated matches the units outside of the literature definition. It is unclear whether this is true or a better interpretation of the permeability calculated; therefore, the original definition postulated by Barton et al. (1985) (i.e. $e^2 = L^2$) is used within this thesis for calculating k . It is also important to mention a deviation of the equation used within this thesis from that of the literature. Barton and de Quadros (1997) defined the semi-empirical flow law relating correlated surface roughness within a fracture to permeability as

$$k = 8175 \left[\frac{JRC^{2.5}}{(E/e)^2} \right]^2 \cdot 10^{-8} \text{ m/s} \quad (8)$$

but it is decided to use ³

$$k = \frac{g}{12\nu} \left[\frac{E^2}{JRC^{2.5}} \right]^2 \cdot 10^{-12} \text{ m/s} \quad (9)$$

where

$$\frac{g}{12\nu} = 817500 \neq 8175 \text{ (ms)}^{-1}$$

As well as uncertainty regarding the method and surrounding literature for calculating the permeability of correlated fracture surfaces, there is uncertainty when applying this method to argillaceous material. The literature from Barton et al. (1985), Barton and de Quadros (1997), and Zou (2020) does not mention equation applicability to dynamic systems and processes, and thus it is inferred that equation (9) is meant for static fractures. In other words, the equation to calculate permeability k is meant for fractures whose surface morphology, and subsequently roughness, does not change as a result of fluid flow within the fracture. This is not the case for argillaceous material as the geomaterial swells upon interaction with water, thus changing the morphology. The change in morphology consequently changes the surface roughness and also makes the fracture surfaces more uncorrelated. Induced fractures within the excavation damage zone (EDZ) are typically formed by tensile stresses and are initially correlated; however, the method of quantifying fracture permeability, within the context of swelling in argillaceous material, is used in a dynamic setting and is neither completely described by the correlated or uncorrelated state. As such, the permeability calculated under these dynamic conditions will likely hold error. To reduce the uncertainty in the hydraulic conductivity calculated along the x and y-axis (i.e. k_x and k_y), a statistical analysis can be carried out to determine whether the surfaces are correlated or not. By correlating all of the profiles of each surface along a particular axis α , a value is derived that indicates the degree of correlation ρ along that particular axis. If $|\rho| > 0.5$, then the surface along α is correlated and the hydraulic conductivity k_α is calculated using equation (3). If $|\rho| \leq 0.5$, then the surface along α is uncorrelated and then the hydraulic conductivity k_α is calculated using

$$k = \frac{g}{12\nu} e^2 \left[1 + c_1 \left(\frac{r_a}{2e} \right)^{1.5} \right]^{-1} \quad (10)$$

³Barton and de Quadros (1997) equate equations (8) and (7), which does not match. Taking the unit definition as stated within the literature, the substituted term has units of L^2 , more specifically μm^2 (Barton et al., 1985; Barton and de Quadros, 1997). Equation (8) is two orders of magnitude higher than it should be, and thus is not used within this thesis to calculate permeability as a function of correlated surface roughness. Though, take note that equation (8) within the literature may simply be a typo.

where r_a is the height between the highest peak and the lowest valley of the surface and c_1 is an arbitrary constant that depends on the author (Barton and de Quadros, 1997; Zambrano et al., 2019).

4.2 Uncertainties in Quantifying Surface Area

The surface area is quantified by utilizing Delaunay Triangulation through the *SciPy* library, which produces tetrahedrons when used with a 3-dimensional data set. The process of triangulation results in stacked tetrahedrons of no known orientation or size, resulting in triangulated surface that cannot be easily quantified for surface area. As such, certain assumptions were made in order to make the quantification happen. It is assumed that there are no internal tetrahedrons produced by triangulation, the outer surface is composed of only one face from each tetrahedron, and that the outer face is correlated to the highest vertex of each tetrahedron. In reality, these assumptions are not verifiable facts, which produces errors within the final quantification of surface area. It is not known which face is the true face that appears on the outer triangulated surface or whether the face itself is related to the highest vertex of each individual tetrahedron. Furthermore, triangles made between uncorrelated peaks or valleys result in erroneous data that may be included within the surface area calculation when not properly filtered out. As such, there is an unknown percentage of derived data that is falsely attributed towards the true value of sample surface area, thereby increasing the uncertainty of the quantified results for surface area of a rough surface.

4.3 2D and 3D Descriptor Analysis

A goal of the method is to identify and analyze morphological descriptors of a rough surface in multiple dimensions to capture the full breadth of necessary data that produces a sufficient characterization of a discrete fracture. Thus, descriptors were analyzed in 2 and 3 dimensions to compare which dimension of analysis is more useful in the fracture characterization. Using the results of the method and the interpretation of Opalinus clay samples 1 and 2, it is observed that neither one form of analysis is inherently better to the other. The bearing area curves (BAC) analyzed per profile along the x and y-axis contains more information on the structure of macroscopic roughness in a sample than its 3D counterpart, allowing for easier interpretation and identification of local heterogeneity. Figure 14 for Opalinus clay sample 2 clearly shows the flatter depression found at the bottom-left corner of the sample, while also showing the increasing trend of macroscopic roughness for both x and y. This is necessary information that presents a complex 3-dimensional structure not adhering to a uniform global undulation. A 3-dimensional BAC shows a general structure of roughness through the shape of the profile, but provides no new information that cannot be obtained from the 2-dimensional data. A 3D BAC contains similar information, though at a lower resolution, and is supplementary information to 2D BAC and amplitude analysis.

The amplitude density quantification and visualization (e.g., Figure 11) are useful pieces of information, showing the spacing, distribution, and cluster size of peaks and amplitude throughout the sample surface for high and low amplitudes. The relative spacing between peaks or between valleys provides a quantified indication as to whether microscopic roughness is uniformly distributed or shows preferential localization of roughness. A 3-dimensional version of amplitude density analysis was attempted to remove the artifacts of "streaking" from the data, but was not successfully done within the time limit of this thesis and presented problems with calculated mean planes. The "streaking" artifact is found within any 2-dimensional analysis utilizing an imaginary line to distinguish the elevation at which a certain percentage of area is underneath the line (e.g., the mean line). This boundary is statistically non-robust and greatly influences the subdivision of data within a surface roughness profile. A clear example is the large streak artifact centered at $y = 1.5\text{mm}$ in Figures 19 and 16 subplot (b). This artifact is the result of the deep valley that is centered at $(x,y) = (2,1.5)\text{mm}$ in Opalinus clay sample 2. The depth of this valley negatively influences the rest of associated profiles and falsely classifies the majority of the profile as a high amplitude peak, which obscures any data and interpretation that could have been made. As a 2-dimensional analysis is done along both the x and y-axis⁴, data from profiles in both directions are effectively useless in accurate interpretation of the surface, and must be ignored within their own respective direction. For example, profiles in the x-axis (i.e. constant x-value with differing y-values) associated with the aforementioned cavity in Figure 18 cannot be used in interpretation for results varying along the

x-axis, but can be used in interpretation for results varying along the y-axis as the profiles in the x-axis are not disturbed by the cavity. In this way, information can still be gleaned from profiles associated with large cavities for either amplitudes or amplitude density. To a lesser extent, the same must be done for all other profiles in both directions of analysis as each profile is influenced by peaks and valleys of larger amplitude. This smaller version of streaking is apparent in all visualizations of 2-dimensional analysis (e.g., surface material in the upper-left corner of Figure 9 is classified as peaks in subplot (a), but are classified as valleys in subplot (b)). As such, it is recommended to use the 3-dimensional amplitude analysis over the 2-dimensional amplitudes as the manual interpretation is easier to understand. The 3-dimensional analysis is also subject to influence from large amplitudes, but the influence is globally applied and so the data within relation to each other remains consistent. That being said, the effect of asperities and valleys on the mean line or plane alter with increasing size of the analyzed sample. If no additional outlying data is included by expanding the range of analysis for the sample, then the mean line or plane will move towards the true mean value. Since the mean line is a non-robust method, this is expected behavior.

4.4 Future Development

As the first version of this method, there are many aspects to improve upon in order to make this method of fracture characterization with morphological descriptors more powerful in computation and usability. One such aspect is to improve the functionalities of the method to influences of normal and shear stresses on the asperity contacts on the hydraulic conductivity of the modeled fracture. Morphological descriptors can be analyzed in time for changes due to swelling as well as effective stresses, but the largest bulk of the method that needs to be improved is computational efficiency and data visualization. As it currently stands, the method takes 30 to 40 minutes to fully run and visualize the data for amplitude, amplitude density, bearing area curves, surface area, and hydraulic conductivity. For a sample size of one or 2 fracture surfaces, the computation of the current method is an insignificant factor that requires limited development and improvement; however, if the method is to be utilized for larger data sets of fracture surfaces, the processing time will take several hours and is a bottleneck. For version of the code to be more powerful and applicable to a larger sample size of fracture surfaces, the visualization for manual interpretation is a moot point. Automatic machine interpretation is needed to process the larger sample size efficiently, for which computational power and efficiency is needed.

There is also the matter of comparability between samples with an increased amount of analyzed samples that must be addressed. For a limited data set, the results derived from the current method is more adept at analyzing the heterogeneous behavior of morphology and surface area within a fracture and so is limited in its capacity to analyze and compare across multiple samples. As such, the maps of data that is used within this thesis to characterize a discrete fracture must be changed so that a small set of data points are produced by the method⁵. Turning the maps of data from the morphological descriptors into one data point for roughness is not possible for data derived from this method; however, a representative value for each morphological descriptor is possible. A possible method of achieving this is to remove outlying data from the data maps and make a probability distribution from the remaining data to derive the mean μ and standard deviation σ . Using μ and σ , a best value with the uncertainty can be used for morphology comparison across multiple samples. Additionally, this representative value may be used within a fracture modelling approach as a roughness parameter, though this is dependent upon the functionality of the model and how the morphological descriptors are used to represent the fracture roughness.

As well as implementing machine interpretation for larger sample sizes, another avenue for development is to improve the process of surface area calculation for a triangulated rough surface with $N \times N$ dimensions. A larger sample area for a singular fracture surface will also act as a bottleneck for computational efficiency of the method, specifically for Delaunay Triangulation. OPA samples 1 and 2 used

⁴The decision to use the x and y-axes in order to 2-dimensionally analyze profiles and data within the data set is a matter of convenience. Diagonal profiles can be used as well in the analysis of the morphological descriptors but prove to be harder to implement into the code and will lead to variable lengths among the profiles. In the case of JRC calculation this is problematic as limited restrict the use of JRC to specific areas of the analyzed sample, further reducing where the permeability calculations are applicable.

⁵This is only needed for morphology as the hydraulic conductivity is already expressed by two values and the surface area can be represented by the calculated total surface area.

matrices of 1550×2088 and had $21 \cdot 10^6$ tetrahedrons for processing before filtering is applied. An expansion of the sample area to be analyzed is expected to significantly increase the amount of data to be processed, which will in turn increase the processing considerably. A faster method of processing the data is needed, perhaps by vectorization, as well as filtering out irrelevant tetrahedrons that do make up the surface of triangulated rough surface. It must be determined as to whether the internal tetrahedrons are produced by the Delaunay triangulation for a rough surface, as well as how to remove these tetrahedrons. The method as it currently stands assumes that one of the triangular faces associated to the highest vertex of a tetrahedron is the true face that comprises the outer surface, but this must be verified and, if possible, improved to automatically determine the true face. It is expected that this will be computationally taxing and more complicated than the code used to development the current stage of the method.

In improving these or other areas of the method, a more powerful and robust method will be developed that can be used to provide a quantified characterization of an individual fracture. This in turn, will aid in the research of self-sealing artificially-induced fractures in argillaceous material, by creating a database of analyzed fractures that displayed self-sealing under a certain set of conditions. In time, this will create an empirical database from which the conditions needed for self-sealing behavior can be predicted and used within the field.

5 Conclusion

It is the aim and intent of this research to develop a method quantifying hydraulic conductivity, surface area and roughness, thereby characterizing a discrete fracture with morphological descriptors. To achieve this a series of steps are taken.

1. Morphological descriptors are identified and related to macroscopic and microscopic roughness as defined relative to the influence of asperities and valleys in the profile.
2. Morphological descriptors are analyzed in 2 and 3-dimensions to compare and determine which dimensions of analysis per morphological descriptors is more appropriate for the developed method of characterization at this stage.
3. A functioning code was built to analyze and quantify morphological descriptors, calculate the surface area of a Delaunay triangulated rough surface, and calculate the hydraulic conductivities k_x and k_y of a correlated modelled fracture with a uniform mechanical aperture of $5 \mu m$.

From the data derived from the characterization method, the following conclusions were made.

- The 2-dimensional bearing area curve data is of higher resolution and more definitively indicates change of macroscopic roughness across the surface in either axis
- The 2-dimensional analysis of the amplitude and amplitude density descriptors are locally defined by the relevant mean line as opposed to the global influence of a mean plane. As such, interpretation of the data maps of these morphological descriptors is more difficult to understand than that of the 3-dimensional counterparts.
- With the current stage of the characterization method, it is recommended to use the 3-dimensional amplitude analysis and the 2-dimensional amplitude density analysis to interpret heterogeneous behavior within a discrete fracture or across two discrete fractures

Future research into fracture characterization by morphological descriptors, surface area, and the hydraulic conductivity should focus on improving the computational efficiency of the code, applying machine interpretation applicability by reducing the data maps into single values, and improving the surface area calculations from the Delaunay triangulation. From these conclusions and recommendations for research, it is hoped that the developed method will become more powerful and useful in providing insight into the self-sealing behavior of swelling argillaceous material. As it stands now, the method of fracture characterization allows insight into the heterogeneous behavior of swelling and the influence of morphology of its development. Continued use may allow for an empirical understanding of the effect of fracture morphology on the self-sealing development and capabilities of artificial fractures in argillaceous material.

A Opalinus Claystone Samples

Opalinus Clay

of the Mont Terri underground laboratory, St-Ursanne

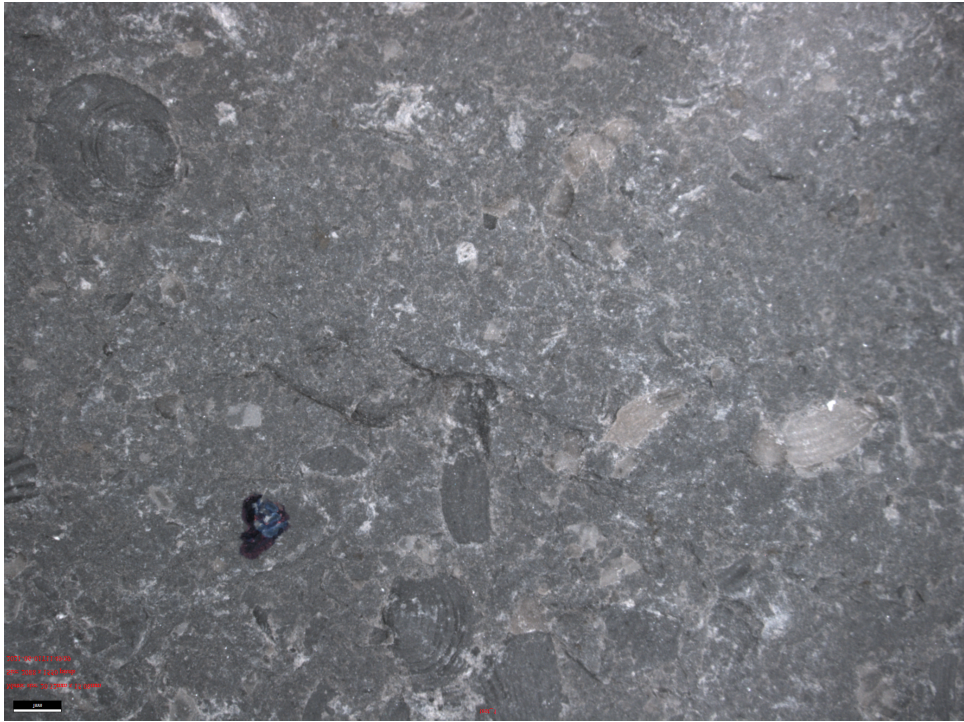
Opalinus clay formed about 175 million years ago. The sedimentation period of this clay deposited on the bottom of a shallow sea and lasted about 400,000 years. This sea covered much of central Europe.

Clay minerals (non-swelling): chlorite, kaolinite	55% by weight
Clay minerals (swelling): illite/smectite	10% by weight
Quartz	20% by weight
Calcite	10% by weight
Feldspar	4% by weight
Organic Carbon	<1% by weight
Total Porosity (water evaporated to 105 C)	12-18%
Hydraulic conductivity	$2 \cdot 10^{-13}$ m/s
Seismic speed of the compression wave	2100-3100 m/s
Swelling Capacity (Perpendicular to stratification)	7-9%
Pore water mineralization	5-20 g/l

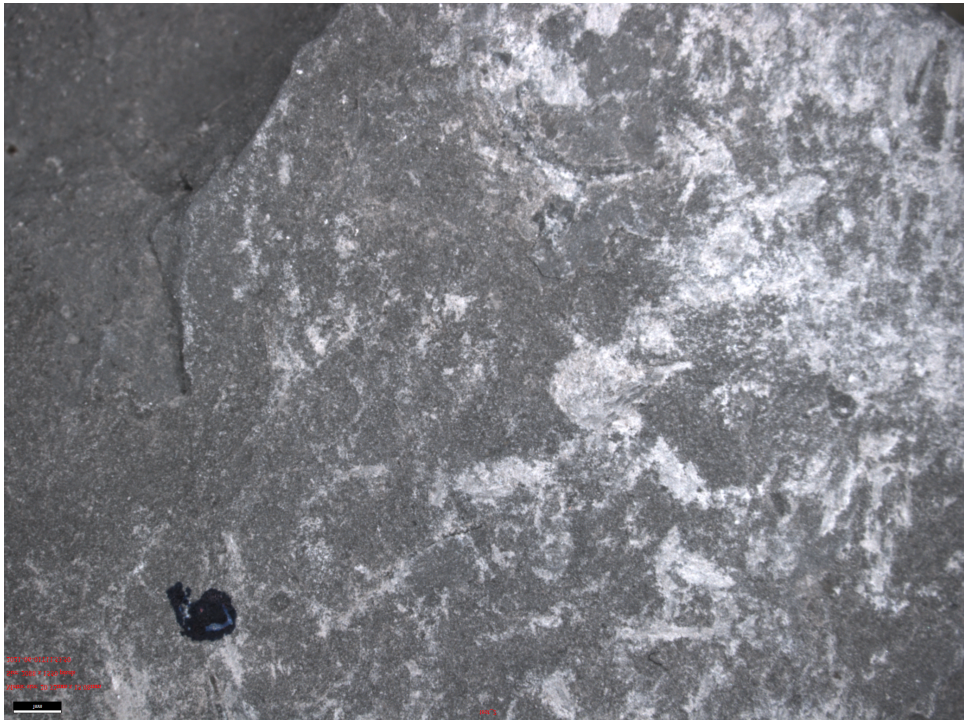
On contact with water, a dry sample of Opalinus Clay swells and disintegrates. If you dry and wet the rock several times, it turns into clay paste.

Table 1: *Translated information from the sample container about the Opalinus clay from the Mont Terri underground laboratory in St-Ursanne. The information includes geological history, typical composition by weight, and swelling behavior.*

Sellin2014



(a) *Opalinus clay sample 1 at mm scale resolution.*



(b) *Opalinus clay sample 2 at mm scale resolution.*

Figure 24: Millimeter scale resolution pictures of the *Opalinus* clay samples obtained from the optical microscope.

B Graphical Relationships

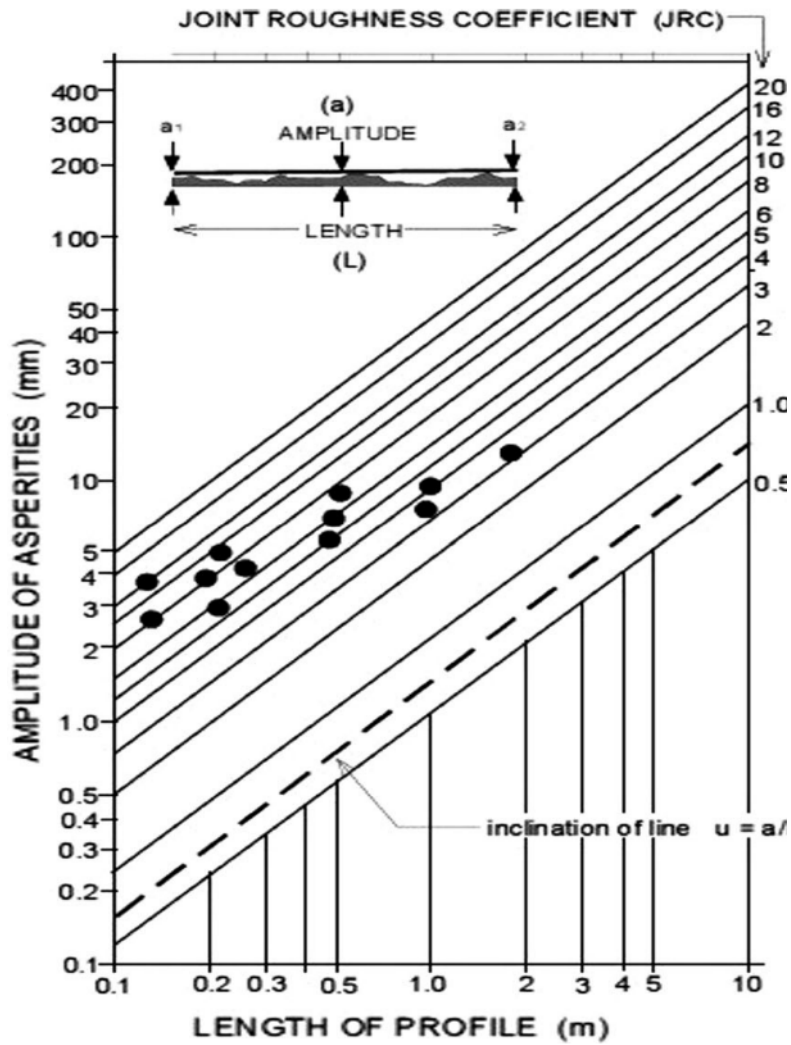


Figure 25: Field data derived relation between the joint roughness coefficient, the max amplitude of roughness profile a_{max} , and the linear length of a roughness profile L . Figure obtained from Morelli (2013).

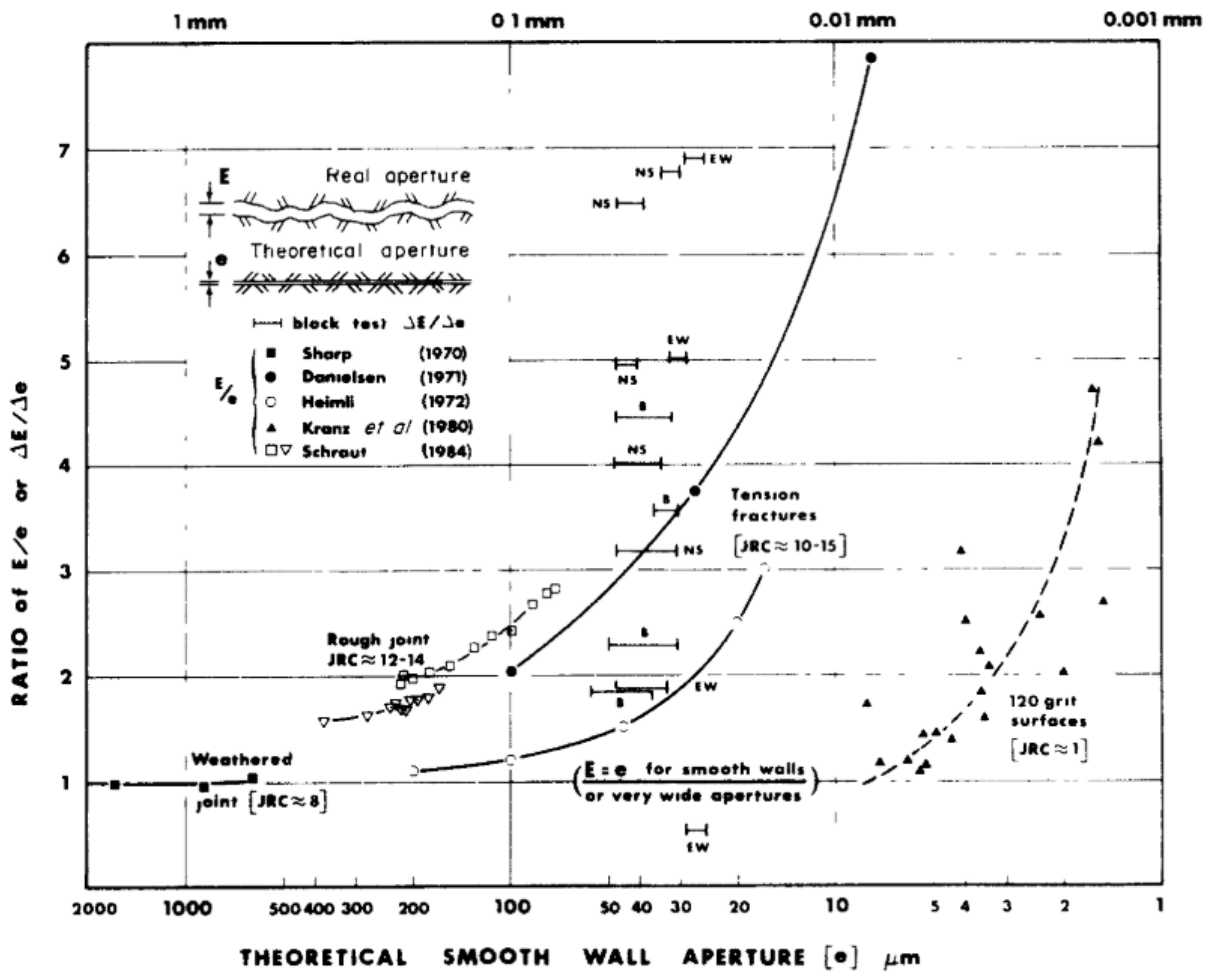


Figure 26: Figure from Barton et al. (1985) showing the divergent behavior between E and e as the value of e changes using experimental data. The difference between the theoretical hydraulic aperture e and the physical aperture E is depicted in the top left corner.

References

- Akono, A.-t., & Kabir, P. (2016). Microscopic fracture characterization of gas shale via scratch testing. *Mechanics Research Communications*, 78, 86–92.
- Barton, N. (1982). *Modelling rock joint behavior from in situ block tests: Implications for nuclear waste repository design* (ONWI-308). prepared by Terra Tek, Inc. for Office of Nuclear Waste Isolation, Battelle Memorial Institute, Columbus, OH.
- Barton, N., Bandis, S. C., & Bakhtar, K. (1985). Strength, Deformation and Conductivity Coupling of Rock Joints. *International Journal of Rock Mechanics Mining Sciences*, 22(3), 121–140. [https://doi.org/10.1016/0148-9062\(85\)93227-9](https://doi.org/10.1016/0148-9062(85)93227-9)
- Barton, N., & Choubey, V. (1977). The Shear Strength of Rock Joints in Theory and Practice. *Rock Mechanics*, 10(1-2), 1–54. <https://doi.org/10.1007/BF01261801>
- Barton, N., & de Quadros, E. F. (1997). Joint aperture and roughness in the prediction of flow and groutability of rock masses. *International Journal of Rock Mechanics Mining Sciences*, 34(3-4), 252.e1–252.e14. [https://doi.org/10.1016/S1365-1609\(97\)00081-6](https://doi.org/10.1016/S1365-1609(97)00081-6)
- Bhushan, B. (2000). Surface roughness analysis and measurement techniques. *Modern Tribology Handbook: Volume One: Principles of Tribology*, 49–119. <https://doi.org/10.1201/9780849377877-10>
- Bock, H., Dehandschutter, B., Martin, C. D., Mazurek de Haller, A., M., Skoczylas, F., & Davy, C. (2010). *Self-sealing of fractures in argillaceous formations in the context of geological disposal of radioactive waste: Review and Synthesis*.
- Corkum, A. G., & Martin, C. D. (2007). The mechanical behaviour of weak mudstone (Opalinus Clay) at low stresses. *International Journal of Rock Mechanics Mining Sciences*, 44(2), 196–209. <https://doi.org/10.1016/j.ijrmms.2006.06.004>
- Danielsen, S. (1971). *Joint permeability* (Doctoral dissertation). Thesis (in Norwegian), Norwegian Technical University, Trondheim.
- Gaucher, E. C., Waber, H. N., Pearson, F., Arcos, D., Bath, A., Boisson, J., Fernandez, A., Gabler, H., Gautschi, A., Griffault, L., & Hernan, P. (2003). Rock and Mineral Characterisation of the Opalinus Clay Formation. In F. Pearson, D. Arcos, A. Bath, J. Boisson, A. Fernandez, H. Gabler, A. Gautschi, L. Griffault, P. Hernan, & H. N. Waber (Eds.), *Mont terri project: Geochemistry of water in the opalinus clay formation at the mont terri rock laboratory* (pp. 281–303). Federal Office of Water; Geology (FOWG).
- Heimli, P. (1972). Water and air leakage through joints in rock specimens. *Fjellsprengningsteknikk, Bergmekanikk, Oslo*, 137, 142.
- Kneucker, T., & Furche, M. (2021). Capturing the structural and compositional variability of Opalinus Clay : constraints from multidisciplinary investigations of Mont Terri drill cores (Switzerland). *Environmental Earth Sciences*, 80(11), 1–21. <https://doi.org/10.1007/s12665-021-09708-1>
- Lauper, B., Zimmerli, G. N., Jaeggi, D., Deplazes, G., Wohlwend, S., Rempfer, J., & Foubert, A. (2021). Quantification of Lithological Heterogeneity Within Opalinus Clay : Toward a Uniform Subfacies Classification Scheme Using a Novel Automated Core Image Recognition Tool. *Frontiers in Earth Science*, 9(May), 1–25. <https://doi.org/10.3389/feart.2021.645596>
- Levasseur, S., Collin, F., Daniels, K., Dymitrowska, M., Harrington, J., Jacobs, E., Kolditz, O., Marschall, P., Norris, S., Sillen, X., Talandier, J., Truche, L., & Wendling, J. (2020). *Deliverable 6 . 1 : Initial State-of-the-Art on Gas Transport in Clayey Materials* (tech. rep. No. 847593). EURAD.
- Morelli, G. L. (2013). On Joint Roughness : Measurements and Use in Rock Mass Characterization. *Geotechnical and Geological Engineering*, 32(2), 345–362. <https://doi.org/10.1007/s10706-013-9718-3>
- Patterson, J. R., Cardi, M., & Feigl, K. L. (2020). Geothermics Optimizing geothermal production in fractured rock reservoirs under uncertainty. *Geothermics*, 88(July). <https://doi.org/10.1016/j.geothermics.2020.101906>
- Pluymakers, A., Kobchenko, M., & Renard, F. (2017). How microfracture roughness can be used to distinguish between exhumed cracks and in-situ flow paths in shales. *Journal of Structural Geology*, 94, 87–97. <https://doi.org/10.1016/j.jsg.2016.11.005>
- Schrauf, T. W. (1984). Relationship between the gas conductivity and geometry of a natural fracture. <http://hdl.handle.net/10150/191812>

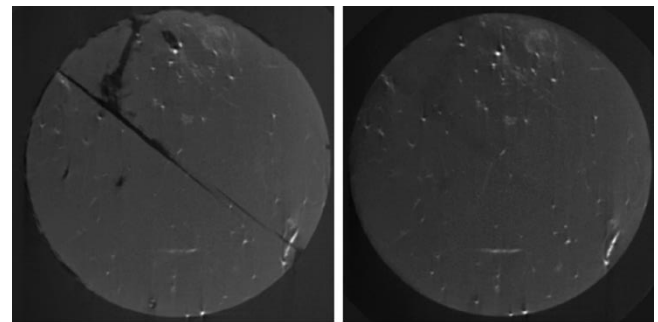
- Sharp, J. C. (1970). *Fluid Flow Through Fissured Media* (Doctoral dissertation). Imperial College London. <http://hdl.handle.net/10044/1/16690>
- Tatone, B. S. A., & Grasselli, G. (2015). Characterization of the effect of normal load on the discontinuity morphology in direct shear specimens using X-ray micro-CT. *Acta Geotechnica*, 31–54. <https://doi.org/10.1007/s11440-014-0320-5>
- Zambrano, M., Pitts, A. D., Salama, A., Volatili, T., Giorgioni, M., & Tondi, E. (2019). Analysis of Fracture Roughness Control on Permeability Using SfM and Fluid Flow Simulations : Implications for Carbonate Reservoir Characterization. *Geofluids*.
- Zou, L. (2020). Inference of Transmissivity in Crystalline Rock Using Flow Logs Under Steady [Please insert \PrerenderUnicode{ã} into preamble] State Pumping : Impact of Multiscale Heterogeneity. *Water Resources Research*, 55, 1–15. <https://doi.org/10.1029/2020WR027254>

Project Title:

Characterisation of crack surface in clay-rich rocks

Introduction

Deep geological disposal constitutes one of the most promising solutions for the safe isolation of high-level and intermediate-level radioactive waste. During the tunnel excavation process, stress concentration around the tunnel leads to the formation of an excavation damaged zone (EDZ), concentrating cracks and fractures. In this zone, a significant increase in hydraulic permeability is observed, which may alter the safety function of the host formation by creating preferential pathways for the migration of radionuclides. However, clay-rich rocks are characterized by an important self-sealing capacity, leading to a reduction in fracture permeability with time. This phenomenon, which is observed in the field and in the laboratory, is not fully understood yet.



Self-sealing of Boom Clay samples (Bastiaens et al., 2007)

Goals

To further the understanding of the self-sealing phenomena within clay-rich rocks, fracture faces must be characterized and analyzed to understand and observe the effects of fracture faces on the self-sealing properties of clay-rich rocks. To that end, a quantified characterization of clay-rich fracture faces will be developed and modified from existing standards for use in understanding the relationship between fracture types and self-sealing capabilities. The objectives of the project are to:

1. Critically review (quantitative) indicators that can be used to characterise surface properties
2. Use relevant indicators to analyse microscope images of cracks in clay-rich rocks

Supervisor(s):

1. Dr. Anne-Catherine Dieudonné
2. Dr. Auke Barnhoorn

More Information:

Name: Dr. Ir. Anne-Catherine Dieudonné
Room: 00.490
Tel.: (+31) (0)15 278 6134
E-mail: a.a.m.dieudonne@tudelft.nl